Design of topological elastic waveguides

M. Miniaci, R. K Pal

Design of topological elastic waveguides

M. Miniaci[1] and R. K. Pal[2, a)]

[1)] *CNRS, Centrale Lille, ISEN, Univ. Lille, Univ. Valenciennes, UMR 8520 - IEMN, F-59000 Lille, France*

[2)] *Mechanical and Nuclear Engineering Department, Kansas State University, Manhattan, Kansas 66503, USA*

(Dated: 22 November 2021)

Topological physics is emerging as an active area of research, addressing fundamental questions on how geometry, symmetry and topology affect physical properties, paving the way towards novel technological applications. Originally investigated in quantum systems, these concepts have been thereafter translated across diverse domains including, electromagnetic, plasmonic, elastic and acoustic waves. Specifically, in elasticity, due to the strong tendency to hybridize of wave modes with different polarization, topological protection is viewed as a revolutionizing approach to design waveguides supporting unique features such as (i) being immune to defects and (ii) suppressing back-scattering during the wave propagation phenomenon. These novel features arise as a consequence of their dispersion surface topology.

This tutorial aims to introduce the theoretical, numerical and experimental frameworks to investigate topological elastic waveguides, discussing the key ideas, first, in the context of discrete systems, and then, in continuous elastic solids. After a comprehensive description of the currently used state of the art scientific techniques, various classes of topological wave phenomena leading to localized waves in elastic architected plates and beams are presented. Implications of the presence of both longitudinal and shear waves in elastic solids are discussed, and the associated challenges, opportunities and strategies to exploit their interplay highlighted. The symmetry conditions required to induce them are discussed using a number of representative examples. Finally, future research directions of this fledgling field are outlined.

[a)] Corresponding author: rkpal@ksu.edu

I. INTRODUCTION

A waveguide is a structure that guides waves with minimal loss of energy by restricting the transmission of energy to one direction. Waveguides in diverse areas of physics exist depending on the kinds of energy they transport, e.g., elastic, acoustic, electromagnetic, plasmonic and electronic. The governing equations associated to the type of wave propagation vary accordingly. For example, wave propagation in elastic media is governed by the Cauchy equations of elastodynamics, in fluids by the Helmholtz equation, while Maxwell and Schrödinger equations govern electromagnetic waves and electron transport, respectively. Note that these equations are distinct in nature, with the Cauchy, Helmholtz and Maxwell equations being systems of hyperbolic partial differential equations while the Schrodinger equation is dispersive[1]. The common link between them that is relevant to the present topic is the existence of wave-like solutions in periodic domains that obey the Bloch theorem[2–4].

There are key differences between wave types supported in various physical media. Elastic solids support both longitudinal (pressure) and transverse (shear) waves. In contrast, fluids support only longitudinal waves[5] while electromagnetic media only support transverse waves[4]. Elastic waveguides have been extensively investigated both to understand the fundamental properties of materials and for technological applications including sensing, actuation, signal processing and energy conversion or harvesting, to name a few[6,7]. For instance, sensing applications may include pressure, temperature and strain measurement. Such waveguides are generally comprised of a straight channel, embedded with piezoelectric transducers. If the length of the channel, and thus the spacing between the embedded transducers changes, then the frequency of the traversing wave also changes. This shift in frequency is correlated with the quantity to be measured. Wave steering for actuation, energy harvesting, vibration control and structural health monitoring are other widespread applications of elastic waveguides[7,8].

In this context, over the last two decades, architected materials or metamaterials[9] have lead to a new class of waveguides exhibiting unique wave control opportunities. For instance, Fig. 1 presents an example of an elastic metamaterial-based waveguide showing energy redirection features. The system consists of a plate with periodic circular inclusions arranged in a square lattice. Due to the periodicity, the waveguide does not allow propagation of waves

in certain band of frequencies, often referred to as *frequency bandgaps*[9]. In this band, the wave is confined to the strip (straight or L-shaped as illustrated). This example illustrates how designing the geometry of the structure can lead to waveguiding along specific paths.

Although the metamaterial paradigm represented an excellent candidate to boost waveguide applications, in fact they have not found widespread technological diffusion. The primary reason is that their unique behavior is sensitive to the presence of defects and imperfections. In particular, significant losses arise due to scattering and localization at defect locations or at corners, as illustrated in Fig. 1b. To overcome these problems, recently, a new class of architected structures called *topological waveguides* have been introduced, rapidly evolving as a leading field of research. Such structures exploit the symmetry and topology of their dispersion surfaces to support modes that are immune to defects, to imperfections and that do not suffer from scattering losses. This immunity arises as a consequence of topological properties, and hence these waves are called *topologically protected*. Originally discovered in $2D$ electron gases in the context of the quantum Hall effect[10], they have been extended to other classical areas of physics in the past decade. Examples include electromagnetic[11], plasmonic[12], acoustic[13], electromechanical[14] and elastic[15–18] media. Even though these diverse media have very distinct governing equations, the concept of topological modes translate across disciplines because the protection arises from specific symmetry properties of the eigenvalue problem[19], or more specifically, a family of eigenvalue problems as a parameter is varied (see sections IV and V, for the details).

Topological modes in elastic media can be broadly classified into two categories. The first one involves active components, like rotating gyroscopes[22,23], and it has been primarily demonstrated for discrete elastic media. The second category solely uses passive components, and has been demonstrated in a wide variety of discrete systems such as combination of pendulums and levers[24], rotating disks[25], mass-spring networks[26–28], as well as for continuous elastic media like architected plates[16,29–31].

This tutorial aims to introduce the fundamental concepts and working principles of such topological waveguides in elastic media, as well as practical steps to design them. It is organized as follows. First, an overview of various waves supported by homogeneous and architected elastic media is presented. This is followed by the description of the most commonly used theoretical, numerical and experimental tools to investigate periodic elastic structures. In section IV, illustrative examples of topological modes are provided using

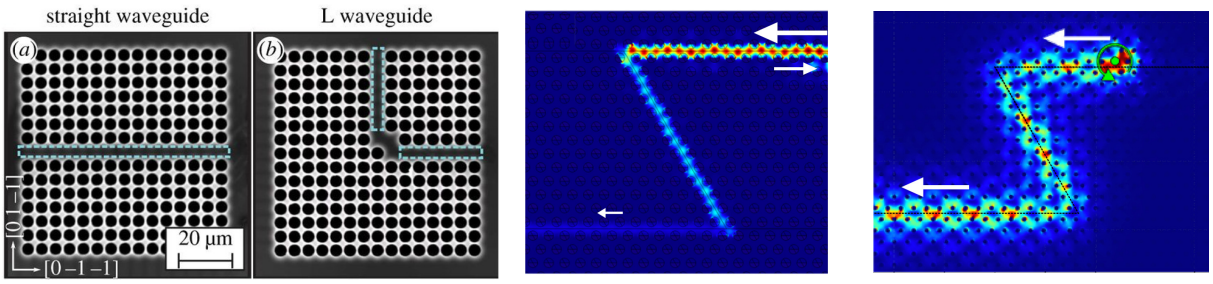

(a) (b) (c)

FIG. 1: (a) Example of waveguides allowing energy to propagate towards (left panel) a straight or (right panel) a L-shaped path[20]. Comparison of the wave field reconstruction for (b) a trivial and (c) a topological photonic waveguide. Wave reflects back at corners in the trivial case while no energy is reflected in the topological one[21]. (Reproduced with permission from Phil. Trans. A 373, 20140364 (2015) and Phys. Rev. Lett. 114, 127401 (2015). Copyright 2015 Royal Society and 2015 American Physical Society.)

discrete mass-spring chains and beams. The key ideas leading to the different types of modes and their combination are described in detail. Section V presents the realization of various topological modes in continuous elastic media and discusses the key steps and strategies for their design. Finally, promising future directions are outlined in Sec. VI.

II. WAVES IN ELASTIC MEDIA

Elastic waves can be defined as disturbances propagating in an elastic solid due to a local deviation from static mechanical equilibrium conditions[32]. Such disturbances manifest as time varying displacement and stress fields in the solid. If the deformations are small enough (i.e., small displacement assumption holds), the medium can be assumed to be linear elastic and the wave characteristics do not depend on the disturbance amplitude. Depending on the domain geometry and boundary conditions (finite or infinite media, presence of free surfaces) of the elastic medium, various types of elastic waves can be identified.

A. Bulk, surface and guided waves in homogeneous media

Waves propagating indefinitely in an infinite homogeneous body without being interrupted by boundaries or interfaces are called bulk waves. The general elastodynamic wave equation governing the evolution of the displacement field $\boldsymbol{u}(\boldsymbol{x}, t)$ has the form

$$\rho \frac{\partial^2 \boldsymbol{u}}{\partial t^2} = \frac{\partial}{\partial \boldsymbol{x}} \left(\mathbb{C} \frac{\partial \boldsymbol{u}}{\partial \boldsymbol{x}} \right) \tag{1}$$

where $\mathbb{C}$ is the fourth-order elasticity tensor and ρ is the density[33,34]. In a linear, isotropic and elastic medium, this governing equation reduces to the form

$$\rho \ddot{\boldsymbol{u}} = (\lambda + \mu) \nabla (\nabla \cdot \boldsymbol{u}) + \mu \nabla^2 \boldsymbol{u}, \tag{2}$$

where λ, μ are the material properties called *Lamé constants*. Solutions to Eqn. (2) support one *longitudinal* wave and two *shear* waves with specific wave velocities that are functions of the material's properties and independent of the frequency or the direction of propagation. These waves have distinct types of motion. Longitudinal waves (also called P-waves) are characterized by particle motion alternating compression and stretching of the medium (see left panel of Fig. 2a). Shear waves are characterized by transverse particle movements in alternating direction (see central and right panels of Fig. 2a). In P-waves, energy propagates parallel to the displacement direction of a point, while in the second one, energy propagates perpendicular to a point's displacement direction. In shear waves, displacement occurs in the plane normal to the propagation direction and the wave can be decomposed into horizontal shear wave (SH) and vertical shear wave (SV), as shown in the central and right panels of Fig. 2a.

Wave propagation in anisotropic media is governed by the general elastodynamics equation Eqn. (1) and their analysis is considerably more complicated. Examples of anisotropic elastic media include piezoelectric media, natural materials like wood, engineered materials like composites. They can be classified as triclinic, monoclinic, orthotropic, cubic and transversely isotropic depending on how isotropy broken along various symmetry axes. Similar to isotropic media, anisotropic media also support three types of waves in an infinite solid. However, there is no clear distinction like longitudinal and shear waves since the particle motion can be at an arbitrary angle to the wave front propagation direction. In addition, this angle and the wave velocity are also direction dependent. The wave front shape is represented by slowness diagrams or surfaces, and they illustrate the variation in wave speed with

direction. Anisotropic media with boundaries can also support Rayleigh and guided waves and their analysis often requires numerical procedures. The interested reader is directed to references discussing elastic waves in anisotropic media[35]. In this tutorial, we will restrict the attention to solids that are isotropic in the bulk at the length scales considered, i.e., macroscopic.

A three-dimensional ($3D$) medium bounded at a surface supports the propagation of waves localized at the free half-space, namely Rayleigh (R) waves and Love (L) waves (refer to Fig. 2b). Rayleigh waves (left panel of Fig. 2b) are characterized by a counterclockwise elliptical motion of the medium particles polarized in the xz plane, if the energy flows along the x direction. The amplitude of these wave decreases exponentially as e^{-bz} with distance z from the free surface. The exponent b is inversely proportional to the wavelength of the wave[33]. Love waves are horizontally polarized surface waves (see right panel of Fig. 2b). They exist only when the top layer has a lower shear wave velocity than the semi-infinite media below it. These waves derive from the interference of many shear waves guided by the top elastic layer, i.e. the one with lower velocity characteristics and with the top boundary free. Particle oscillations in Love waves involve alternating transverse movements. The direction of medium particle oscillations is horizontal (for instance in the xz plane) and perpendicular to the direction of propagation (x). As in the case of Rayleigh waves, their wave amplitude decreases with depth.

Finally, in some materials, the relation expressed by Eqn. (1) does not fully describe their response when subjected to an elastic strain. Indeed, certain materials become electrically polarized when they are strained. This effect, called the direct piezoelectric effect, manifests experimentally by the appearance of bound electrical charges at the surfaces of a strained medium. It is a linear phenomenon, and the polarization changes sign when the sign of the strain is reversed. Though piezoelectricity is a complex phenomena intimately related to the microscopic structure of the solid, the macroscopic behavior can be quantitatively captured in terms of a rather simple constitutive model. We direct the reader interested in wave propagation in piezoelectric media to additional references[36–38].

Let us now discuss wave propagation in structures where one dimension is much smaller than the other two. Examples include plates and shells, where the thickness is smaller compared to the in-plane dimensions. When a point in a plate (Fig. 2c, for example) is transversely excited, waves propagating from this point encounter the upper and lower free

surfaces of the structure, leading to reflection and mode conversion (longitudinal waves to shear waves, and vice versa). The wave field is a superposition of multiple reflections and the resulting generated waves. This wave field can essentially be approximated as propagating in the in-plane directions with a specific displacement field in the direction of the smaller dimension (examples in Fig. 2d). Such waves are called Lamb waves or guided waves.

An elastic plate supports an infinite number of guided modes, each with a different displacement field. Among them, the symmetrical and anti-symmetric zero-order modes (shown in Fig. 2d, having symmetric and anti-symmetric transverse displacement field about the plate center-plane) deserve special attention because (i) they are the only modes that exist over the entire frequency spectrum from zero to indefinitely high frequencies, and (ii) in most practical situations they carry more energy than the higher-order modes. Also, in the low frequency range (i.e. when the wavelength is greater than the plate thickness) these modes are called the "extensional mode" and the "flexural mode" respectively, terms that describe the nature of the particle motion.

Lamb waves are dispersive, i.e., their wave velocities depends on the frequency in addition to the material and geometric properties of the plate. These wave velocities require numerical procedures and cannot be determined in analytical closed form[33,34]. Guided waves travel long distances with little attenuation, making them well suited for non-destructive evaluation and structural health monitoring applications. The word *waveguide* arises from structures hosting these types of waves. The interested reader is directed to references that discuss approaches to extract Lamb wave solutions in isotropic, anisotropic, as well as piezoelectric waveguides[8,33,36].

B. Waves in architected structures

In previous section we have seen that the properties of bulk, surface and guided waves are determined by the relationship between the particle motion, wave propagation direction and the constitutive properties of the medium. In homogeneous, isotropic (infinite) media, the energy flow coincides with the wave front of the wave.

However, in many practical cases, the assumptions of isotropy and infinite extent are not always satisfied, and often waves propagate in media with geometrical or mechanical discontinuities. When the elastic waves propagate in structures with complex geometries,

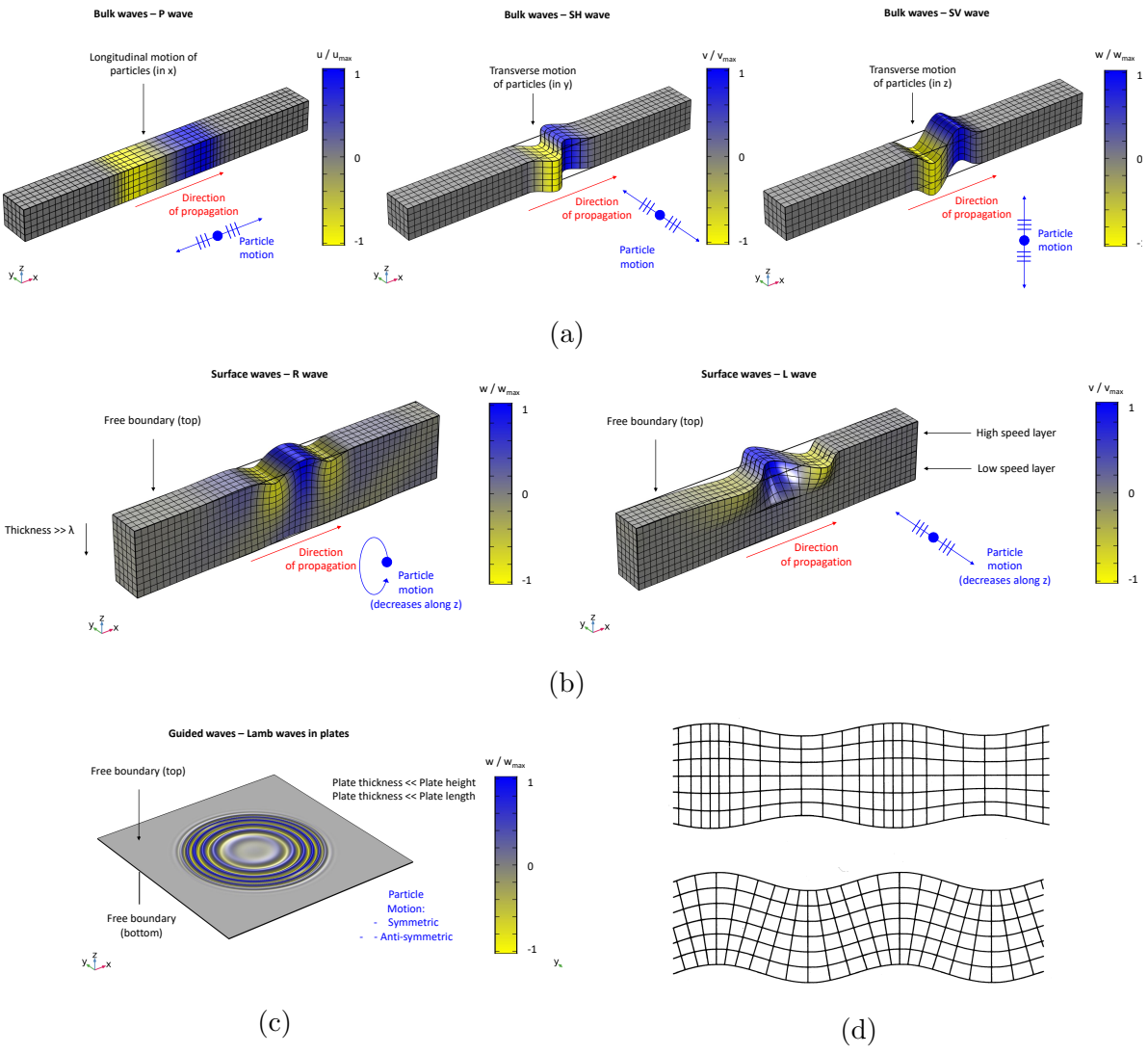

FIG. 2: (a) Bulk Waves propagating in an infinite media and characterized by (left panel) particle motion alternating compression and stretching of the medium, and (center, right panels) transverse particle motion in orthogonal planes. (b) A 3D medium with a free surface allows for the propagation of waves localized at the free half-space. Left panel: Rayleigh waves and right panel: Love waves. (c) Lamb waves in a plate. (d) First two Lamb modes, top: symmetric and bottom: anti-symmetric about the plate center-plane.

multiple reflections take place due to impedance mismatch at the interfaces and free surfaces, strongly complicating the energy flow/redistribution. The most general case is when waves propagate in structures with no spatial inversion symmetry and broken time-reversal symmetry, i.e., where the material parameters and geometrical design of the system randomly vary both in space and time. A mechanical system has broken time reversal symmetry if

its governing equations change under the transformation $t \to -t$. Examples include structures with attached spinning gyroscopes[22,23] and systems with damping. Similarly, spatial inversion symmetry means the structure is invariant under the transformation $\boldsymbol{x} \to -\boldsymbol{x}$. If a certain regularity is assumed for the spatio-temporal modulation (for instance introducing periodicity), the use of the space-time Floquet theory[39–42] can be envisaged. So far, non-reciprocity through space-time modulation has been investigated in optical and electromagnetic systems, in the case of mechanical waves, as well as in airborne acoustics[43–45]. Breaking time-reversal symmetry requires active components that introduce/remove energy into/from the structure.

Another emerging area of research concerns the propagation of elastic waves in solely passive media characterized by a high degree of complexity in their geometrical design. Often periodic, i.e., characterized by a unit cell periodically repeated in space, these media are usually referred to as *architected metamaterials*. The periodic architecture of these structures can be limited to one, two or three dimensions, and be at the same scale (ordinary architected structures)[9] or at multiple scale levels (hierarchical architected structures)[46,47]. Their static and dynamic properties derive from a tailored geometry and material distribution (creating specific impedance jumps/variations), in addition to their material constituents. Compared to waves in conventional materials described in the previous section, architected materials have opened novel ways of manipulating and controlling the propagation of elastic waves. Examples include omnidirectional stop bands or full bandgaps (BGs), negative refraction, wave focusing and perfect transmission of waves at sharp angles[48–52].

Figure 3 reports an example of an architected elastic waveguide, i.e., namely a plate with circular holes in a hexagonal lattice arrangement. The smallest repetitive block, if one exists, is called *unit cell*, and in the considered case is highlighted in light green in Fig. 3a, and reported in its in-plane and trigonometric view in Figs. 3b,c, respectively. The interplay of periodicity, geometry and material composition within each unit cell can result in effective mechanical properties very distinct from those of its constituent materials. The unconventional dynamic properties may derive from (i) Bragg scattering, i.e., a destructive interference arising from an impedance mismatch proportionally periodic in space to $na/2$, with $n \in \mathbb{N}$ and a the lattice parameter[3], or (ii) local resonances[53].

The information about the wave propagation within these structures is often derived through the examination of the so-called dispersion diagram or dispersion surfaces. In what

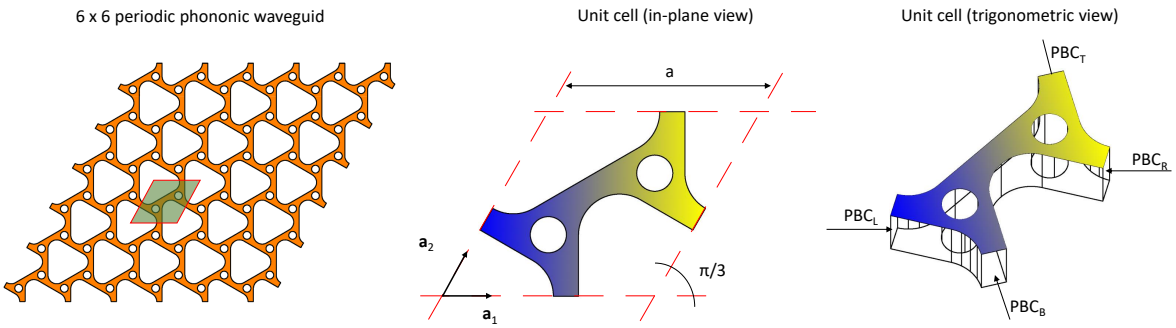

FIG. 3: (a) In-plane view of an architected waveguide consisting of a plate with circular and triangular holes in a periodic arrangement. The unit cell, i.e. the smallest repetitive building block, is highlighted in light green. (b) In-plane and (c) isometric view of the unit cell. $\mathbf{a}_1$ and $\mathbf{a}_2$ are the lattice vectors. Dispersion analysis of this periodic structure is conducted by the imposing periodic boundary conditions (PBC) at the domain edges (see section III B for further details).

follows, the principal approaches to extract these information are presented.

III. METHODS FOR DISPERSION ANALYSIS OF PERIODIC ELASTIC STRUCTURES

Dispersion analysis gives the frequency-wave vector $\omega(\boldsymbol{\kappa})$ relation, i.e., the relation between spatial and temporal periodicity of a traveling wave. An arbitrary wave of sufficient regularity can be expressed as a superposition of harmonic waves of distinct frequencies. Dispersion relation specifies how each individual frequency component propagates in a solid. In particular, it provides information of the wave vector as a function of the frequency and its gradient gives the group velocity of the wave. Dispersion relations completely characterize the dynamic behavior of a linear elastic solid because in conjunction with the superposition principle, they can be used to predict the propagation of any arbitrary wave. In this section, we discuss various methods to determine dispersion relations for an architected linear elastic solid.

A. Analytical techniques

The plane wave expansion method gives a good approximation to the mode shape and natural frequency of an architected elastic media that is periodic. Let us consider a plane wave traveling through a periodic elastic structure with frequency ω and wave vector $\boldsymbol{\kappa}$. The wave vector may be viewed as the spatial analogue of frequency. Just as frequency measures how rapidly a point in the medium is varying with time, wave vector measures how rapidly the displacement field is varying in space. Hence, it is a vector having each component κ_p inversely proportional to the corresponding wavelength along the direction with unit vector $\boldsymbol{e}_p$.

The displacement field due to this traveling wave is expressed as

$$\boldsymbol{u}(\boldsymbol{x},t) = \boldsymbol{U}(\boldsymbol{x})e^{-i\omega t}. \tag{3}$$

In a periodic domain with lattice vectors $\boldsymbol{a}_p$, $\boldsymbol{U}(\boldsymbol{x})$ satisfies the Bloch periodicity condition $\boldsymbol{U}(\boldsymbol{x}+\boldsymbol{a}_p) = e^{i\boldsymbol{\kappa}\cdot\boldsymbol{a}_p}\boldsymbol{U}(\boldsymbol{x})$ for each periodic direction p and $\boldsymbol{U}(\boldsymbol{x})$ is called a Bloch mode. Let us derive an expression for $\boldsymbol{U}(x)$ that will help us to determine the dispersion surfaces. We start by considering the function $\boldsymbol{g}(\boldsymbol{x}) = \boldsymbol{U}(x)e^{-i\boldsymbol{\kappa}\cdot\boldsymbol{x}}$. The Bloch periodicity condition then implies that $\boldsymbol{g}(\boldsymbol{x})$ is periodic in the unit cell, i.e., $\boldsymbol{g}(\boldsymbol{x}+\boldsymbol{a}_p) = \boldsymbol{g}(\boldsymbol{x})$. Indeed,

$$\boldsymbol{g}(\boldsymbol{x}+\boldsymbol{a}_p) = \boldsymbol{U}(\boldsymbol{x}+\boldsymbol{a}_p)e^{-i\boldsymbol{\kappa}\cdot(\boldsymbol{x}+\boldsymbol{a}_p)} = e^{i\boldsymbol{\kappa}\cdot\boldsymbol{a}_p}\boldsymbol{U}(\boldsymbol{x})e^{-i\boldsymbol{\kappa}\cdot\boldsymbol{a}_p}e^{-i\boldsymbol{\kappa}\cdot\boldsymbol{x}} = \boldsymbol{U}(\boldsymbol{x})e^{-i\boldsymbol{\kappa}\cdot\boldsymbol{x}} = \boldsymbol{g}(\boldsymbol{x}).$$

Since $\boldsymbol{g}(\boldsymbol{x})$ is a periodic function with periodicity of the unit cell, it can be expressed as a Fourier series in the form

$$\boldsymbol{g}(\boldsymbol{x}) = \sum_{m,n,r=-\infty}^{\infty} \boldsymbol{a}_{m,n,r}e^{i\boldsymbol{G}_{m,n,r}\cdot\boldsymbol{x}}, \quad \boldsymbol{G}_{m,n,r} = m\boldsymbol{a}_1 + n\boldsymbol{a}_2 + r\boldsymbol{a}_3. \tag{4}$$

Here m, n and r take integer values and $\boldsymbol{a}_{m,n,r}$ is a vector with complex coefficients for each basis function with index (m, n, r). For periodic beams, we only have $\boldsymbol{a}_1$ while for periodic plates, we only have $\boldsymbol{a}_1$ and $\boldsymbol{a}_2$. Using this equation, the displacement field can be written as

$$\boldsymbol{u}(\boldsymbol{x},t) = \sum_{m,n,r} \boldsymbol{a}_{m,n,r}e^{i\boldsymbol{G}_{m,n,r}}e^{i\boldsymbol{\kappa}\cdot\boldsymbol{x}}e^{-i\omega t}. \tag{5}$$

The real part of the right hand side in the above equation gives the displacement field.

Equation (5) is the starting point of the plane wave expansion method. The displacement field can be expressed as a superposition of periodic waves with periodicity of the unit cell,

along with a factor $e^{i\boldsymbol{\kappa}\cdot\boldsymbol{x}}$ that takes into account the wavelength of the wave. The functions $e^{i\boldsymbol{G}_{m,n,r}}$ constitute an orthonormal basis over a unit cell and determine the part of the Bloch mode that fluctuates within the unit cell. To determine the dispersion relation $\omega(\boldsymbol{\kappa})$, we choose a finite set of basis function by allowing m, n, r to take integer values from $-N$ to N in Eqn. (5). The coefficients $\boldsymbol{a}_{m,n,r}$ are determined by substituting the expression for $\boldsymbol{u}(\boldsymbol{x}, t)$ into the governing equations, taking the scalar product with each basis function $\boldsymbol{e}_p e^{i\boldsymbol{G}_{m,n,r}}$ and integrating over a unit cell. Recall that $\boldsymbol{e}_p$ is the unit vector along direction with index p. This procedure leads to a system of linear homogeneous equations defining an eigenvalue problem and its solution gives the dispersion surfaces. In particular, we impose each value of the wave vector and determine the corresponding natural frequencies.

Let us now illustrate the PWE method with an example. Figure 4a displays a metamaterial bar with two alternating materials whose Young's modulus E are different. The darker material has E 4 times higher than the lighter material. The PWE method can be used to calculate the dispersion surfaces of this structure. Figure 4b displays the real part of two basis functions $e^{i(G+\kappa)x}$ for the PWE method with $\kappa = 2\pi/3L$ and $G = 0, 2\pi/L$. Applying this method yields the frequencies and corresponding mode shapes of the propagating waves. The red curve in Fig. 4a shows the displacement field of the first mode shape at a wavenumber $\kappa = 2\pi/3$ over 6 unit cells. For this wavenumber κ, Bloch periodicity condition implies that the displacement field is periodic over 3 unit cells, which is consistent with the curves in Fig. 4a. The reader may refer to additional detailed illustrations on the PWE method for analysis of propagating[54–61] and evanescent[62,63] waves in architected elastic structures.

The analytical plane wave expansion method works well for simple geometries where the mode shape can be represented with a few basis functions N in Eqn. (5). As the unit cells become more complex, incorporating complicated shaped holes or inclusions, the error in mode shape represented with a small N is high, while increasing N leads to ill conditioning of the resulting matrices. To overcome these issues, numerical methods based on finite element analysis are used to efficiently determine the dispersion surfaces for complex geometries. We discuss this method in the following subsection.

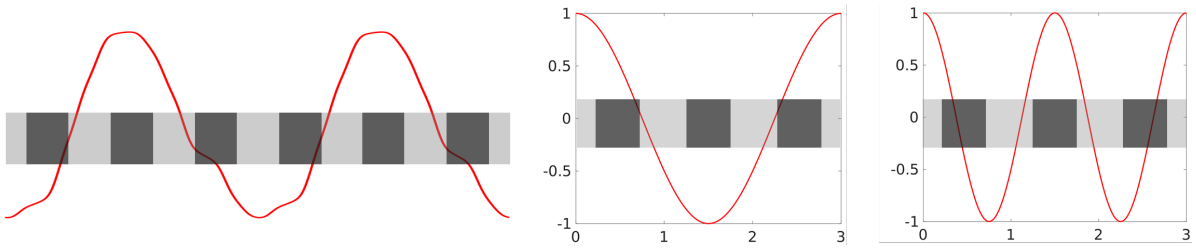

(a) (b)

FIG. 4: (a) Mode shape (red curve) of a metamaterial bar (schematic behind the curve) with two materials of different Young's modulus at a wavenumber $\kappa = 2\pi/3L$. Displacement field is shown over 6 unit cells. (b) Real part of typical basis functions $e^{i(\kappa+G)x}$ in the PWE method with $G = 0$ and $G = 2\pi/L$. Basis functions are shown over 3 unit cells for clarity.

B. Numerical techniques

The governing equation (2) for a $3D$ linear elastic solid is considered over a single unit cell with appropriate boundary conditions to determine the dispersion surfaces. To illustrate these conditions, let us consider the unit cell in Fig. 3c. The displacement fields at the right and top boundary are expressed in terms of the corresponding fields at the left and bottom boundary using Bloch periodicity as

$$\boldsymbol{u}(\boldsymbol{x}_R, t) = e^{i\boldsymbol{\kappa}\cdot\boldsymbol{a}_1}\boldsymbol{u}(\boldsymbol{x}_L, t), \quad \boldsymbol{u}(\boldsymbol{x}_T, t) = e^{i\boldsymbol{\kappa}\cdot\boldsymbol{a}_2}\boldsymbol{u}(\boldsymbol{x}_B, t). \tag{6}$$

Similarly, by force equilibrium at each point on the boundary, the traction $\boldsymbol{t}$ on the various surfaces are related as

$$\boldsymbol{t}(\boldsymbol{x}_R, t) = -e^{i\boldsymbol{\kappa}\cdot\boldsymbol{a}_1}\boldsymbol{t}(\boldsymbol{x}_L, t), \quad \boldsymbol{t}(\boldsymbol{x}_T, t) = -e^{i\boldsymbol{\kappa}\cdot\boldsymbol{a}_2}\boldsymbol{t}(\boldsymbol{x}_B, t). \tag{7}$$

The two equations (6) and (7) constitute independent boundary conditions on each boundary. Substituting $\boldsymbol{u}(\boldsymbol{x}, t) = e^{i\omega t}\boldsymbol{U}(\boldsymbol{x})$ into the governing equations and using these two conditions leads to a well posed eigenvalue problem. Its solution provides the mode shapes $\boldsymbol{U}(\boldsymbol{x})$ and natural frequencies ω for each wave vector $\boldsymbol{\kappa}$. The eigenvalue problem is in the form of a partial differential equation and it can be solved using numerical techniques.

The finite element method (FEM) is the most widely used numerical method for dispersion analysis of unit cells with complex geometries. This method involves two key steps to

convert the governing partial differential equation to a system of algebraic equations[64]. The first step is to consider a weak form of the governing equations that results in a variational problem over a function space. The second step is to reduce this variational problem to a system of algebraic equations by *discretization*, i.e., choosing a finite dimensional subspace that approximates the infinite dimensional function space. Discretization involves two components: (a) meshing, i.e., dividing the domain into smaller sub-domains called elements, and (b) element type, i.e., choosing a set of basis functions up to a specified order for an element. The solution fields in each element lies in the vector space spanned by these basis functions. The mesh should be sufficiently fine with well shaped elements so that the solution can be represented with good resolution using the chosen element type. FEM formulation for dispersion analysis has been done in recent years for beams, plates and solids[65–67]. Today, several commercial software packages are available to conduct dispersion analysis using FEM.

C. Experimental techniques

From the experimental point of view, and focusing our attention on the ultrasonic frequency range, many methods to excite (indicated by "E" for the sake of brevity in this section) and measure ("M") elastic waves are widely used. A non-exhaustive list include: (i) conventional and piezoceramic ultrasonic transducers (E/M); (ii) comb-type ultrasonic transducers (E/M); (iii) electromagnetic acoustic transducer (EMAT), for non-contact acoustic wave generation and reception in conducting materials; (iv) magnetostrictive transducers (E/M), exploiting the property of magnetic materials that causes them to change their shape or dimensions during the process of magnetization; (v) impact-controlled approaches (E), such as instrumented impact hammers; (vi) electrodynamic shakers (E); (vii) optical fiber sensors (M); (viii) photoelasticity (M), describing changes in the optical properties of a material under mechanical deformation; (iix) photothermal (M); (ix) scanning laser Doppler vibrometer - SLDV (M), that determines the out-of-plane or normal velocity at each point on the surface of an elastic structure through the Doppler effect. These techniques, which can be selectively chosen according to the specific type of wave to excite/detect (Rayleigh, Lamb, Shear Horizontal, etc.) and the experimental conditions of measurement, can be separated in two categories: those requiring a contact with the sample and those that are

contactless.

Among the above listed techniques for wave detection, the SLDV is being used increasingly often in recent years for several reasons, especially in the case of architected materials. First of all, SLDV, being a contactless measurement technique, eliminates the detrimental effect of adding additional masses in the measurement locations, which can result in a local change of the structure rigidity. Another advantage of SLDV is its ability to perform measurements automatically in a large number of precisely defined points, almost regardless of the complexity of the geometrical pattern to scan. Also, SLDV allows for 3D measurements, allowing object vibration components to be recorded both in the plane perpendicular to the investigated surface and in the one parallel to it. Finally, SLDV allows automatic measurements on a very dense mesh of measurement points, enabling thus the measurement of a propagating elastic wave with precision, not only in time but also in space. The measurement frequency range is another positive point of this technique, since it allows for measurements from close to 0 Hz to several MHz, as well as a wide range of vibration velocity amplitudes[7]. All these advantages make SLDV one of the most effective measurement techniques for dynamic characterization of architected materials and elastic waveguides. In contrast, it is more difficult to single out a best suited excitation technique and its choice is often a result of several considerations including, (i) frequency range and (ii) type of waves to excite, (iii) geometric and (iv) elastic properties of the specimen to investigate. We direct the reader to reference books[7,8] on these aspects.

IV. OVERVIEW OF TOPOLOGICAL MODES

There are several classes or types of topological modes depending on the type of symmetry that is broken in a lattice[19,68]. As discussed in the introduction, they can broadly be classified into two categories: those that break time reversal symmetry and those that preserve it. This classification is based on the simple observation that an elastic media is symmetric or not under the transformation $t \rightarrow -t$. The physical meaning is that breaking time-reversal symmetry requires active or dissipative components. A more fundamental classification of symmetries involves using time-reversal, chiral and particle-hole symmetry operators is used in quantum mechanics, where each of these has a physical meaning. In an elastic media, applying the corresponding mathematical operators leads to constraint equations that may

not be related to fundamental principles like balance and conservation laws.

We introduce the key concepts underlying topological modes through a number of examples of varying complexity. They are all based on discrete lattices or elastic beams with the goal of elucidating the main ideas behind topological protection in a simplified setting[69,70]. The first example concerns discrete mass-spring chains followed by its extension to continuous elastic media: architected beams. Afterwards, an example presenting lattices with a varying parameter is considered (Sec. IV C), showing energy transport from one corner to another. Sec. IV D presents an example of how topological modes can be induced in $2D$ discrete lattices, and their relation to the concepts in $1D$ lattices are elucidated in Sec. IV A. We will focus on two distinct classes of modes, namely helical and valley modes in $2D$ lattices.

A. Illustrative example: topological modes due to spectral flow

Let us illustrate the key idea behind topological modes with a simple discrete mass-spring chain example. It is inspired by the SSH model, the first model that was demonstrated to support localized electronic modes due to topological properties[10,71]. The corresponding ideas are valid and can be extended to continuous elastic media. Consider the infinite mass-spring chain shown in Fig. 5a, having identical masses m and two springs of different stiffness k_1 and k_2. Note that this chain is a periodic structure. The unit cell of a periodic structure is the smallest unit that generates the lattice by repetitive translation. Identifying a unit cell requires careful consideration to satisfy this lattice generation requirement. The unit cell of this chain has 2 springs (k_1, k_2) and 2 identical masses, labeled a and b.

Let us investigate the dynamic response of the infinite chain. The governing equations for a unit cell indexed n are

$$m\ddot{u}_{n,a} + k_1(u_{n,a} - u_{n,b}) + k_2(u_{n,a} - u_{n-1,b}) = 0,$$
$$m\ddot{u}_{n,b} + k_1(u_{n,b} - u_{n,a}) + k_2(u_{n,b} - u_{n+1,b}) = 0.$$

We solve this system of equations in the Fourier domain by imposing a solution of the form $u_{n,\alpha} = e^{i\mu n - i\omega t}U_\alpha$ with $\alpha = \{a, b\}$. Here μ and ω are the wavenumber and frequency, respectively and U_α are the displacement of the two masses in the Fourier domain. The

above system of equations then become

$$\begin{pmatrix} k_1 + k_2 & -k_1 - k_2 e^{-i\mu} \\ -k_1 - k_2 e^{i\mu} & k_1 + k_2 \end{pmatrix} \begin{pmatrix} U_a \\ U_b \end{pmatrix} = \omega^2 \begin{pmatrix} m & 0 \\ 0 & m \end{pmatrix} \begin{pmatrix} U_a \\ U_b \end{pmatrix} \tag{8}$$

Equation (8) defines an eigenvalue problem and its solution gives the dispersion surfaces of the structure, illustrated in Fig. 5c. For each wavenumber μ, there are two natural frequencies ω that are solutions of Eqn. (8). These surfaces characterize traveling wave solutions in the infinite lattice. Note that there are no real valued wavenumbers μ when Ω is in the range $(1, \sqrt{2})$ and when $\Omega > \sqrt{2}$, which indicates an absence of traveling waves at these frequencies.

Next, let us consider the dynamic behavior of a finite chain. In general, its natural frequencies depends on the chain's boundary conditions. To exemplify the ideas, let us consider a chain in the form of a ring (Fig. 5b) with M unit cells. Each mode shape can be identified with a corresponding traveling wave in the infinite lattice, that satisfies the condition

$$u_{n,\alpha} = u_{n+M,\alpha}. \tag{9}$$

This condition arises in the finite lattice due to the topology of the ring. Let us determine the wavenumber of the corresponding wave in the infinite lattice. Combining this condition (Eqn. (9)) with the Bloch periodicity condition leads to the following set of wavenumbers for a ring with M unit cells

$$u_{n+M,\alpha} = e^{i\mu M} u_{n,\alpha} = u_{n,\alpha} \implies e^{i\mu M} = 1. \tag{10}$$

Note that the solution to $e^{i\mu N} = 1$ is $\mu = 2\pi s/N$ for any integer s. Due to the discrete nature of the lattice, wavenumbers modulo 2π essentially represent the same wave. For example, the displacement field corresponding to waves with wavenumbers μ and $\mu + 2\pi$ are identical. A unique set of waves can be identified with wavenumbers lying in the first Brillouin zone. They are

$$\mu = \frac{2\pi s}{N}, \quad s = 0, \pm 1, \pm 2, \ldots \pm \lfloor N/2 \rfloor. \tag{11}$$

Here $\lfloor N/2 \rfloor$ is the integer part of $N/2$. Hence each mode on the ring can be identified with a wavenumber from the set in Eqn. (11).

The red circles in Fig. 5c display these wavenumber values for a ring with $N = 5$ unit cells. This ring has $2N = 10$ masses and thus 10 natural frequencies. These natural frequencies

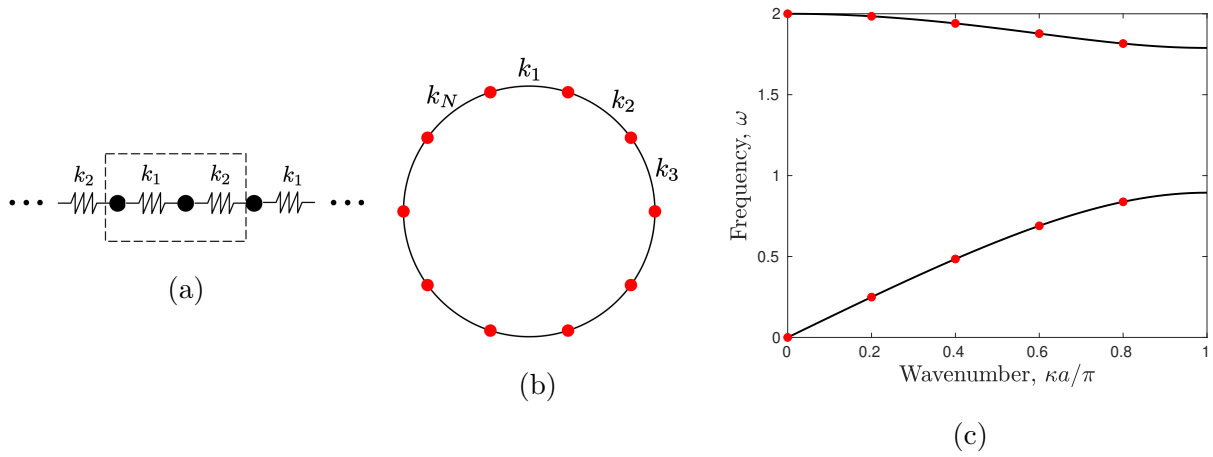

FIG. 5: (a) An infinite lattice with two distinct and alternating spring stiffness values. Dashed rectangle is a unit cell. (b) Hypothetical finite lattice in the form of a ring. (c) Dispersion curves of the lattice along with finite ring frequencies superimposed as red circles.

all lie on the dispersion curves and their corresponding wavenumbers take values in the set derived in Eqn. (10). This set ensures that there are $N = 5$ modes of the ring lattice in each dispersion branch. To summarize, the key observation is that the topology of the ring lattice ensures that equal number of its modes lie on each dispersion branch.

Let us now consider a ring of $N = 40$ masses with two kinds of unit cells, shown in Figs. 6a and 6b. We set the r-th spring stiffness in the ring to

$$k_r = 1 + \alpha \cos\left(\frac{2\pi r}{p}\right), \qquad r \in \{1, 2, \ldots, N\}. \tag{12}$$

Here $\alpha < 1$ and p is equal to the number of masses (or springs) in each unit cell. r is the spring index and it runs from 1 to N as there are N springs in the ring. Setting $p = 4$ and 5 gives the rings whose unit cell schematics are shown in Fig. 6a and 6b. Their corresponding dispersion curves, along with the natural frequencies of the corresponding ring of N masses is also shown below (Figs. 6c, 6d). Let us make a couple of observations that are analogous to the chain with two distinct springs (k_1 and k_2) discussed above. The lattice with $p = 4$ has 4 dispersion curves or branches and the N natural frequencies are distributed equally in each dispersion branch, with the wavenumbers given by Eqn. (10). Similarly, the lattice with $p = 5$ has 5 masses per unit cell, 5 dispersion curves and $N/5$ natural frequencies in each branch.

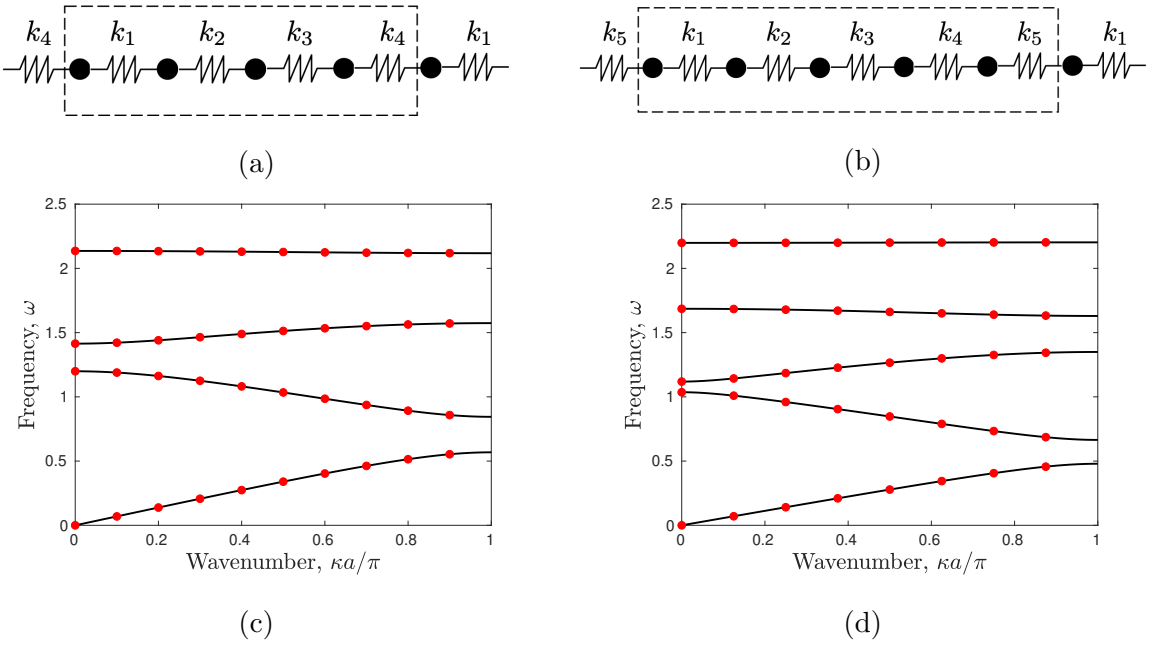

FIG. 6: Unit cells of lattices with (a) 4 and (b) 5 distinct spring stiffness values. Dashed rectangle shows unit cell. (c), (d): their dispersion curves having 4 and 5 branches. Red circles show the frequencies of a finite ring lattice of 40 masses are distributed equally among the dispersion curves: 10 and 8 in each branch, respectively, for the two lattices.

Now, let us examine what happens as we transition from the $p = 4$ to the $p = 5$ lattice. We do this by setting $p = 4+\beta$ in the denominator in Eqn. (12), with β taking values in the set $[0, 1]$. The natural frequencies are given by solving the eigenvalue problem arising from the governing equations for the masses in the ring. Figure 7 displays the natural frequencies of the ring with N masses as a function of β. As β is varied continuously in the set $[0, 1]$, the N natural frequencies also vary continuously. At $\beta = 0$, the $p = 4$ lattice has 4 dispersion bands separated by bandgaps and there are $N/4 = 10$ frequencies in each band. On the other hand, at $\beta = 1$, the $p = 5$ lattice has 5 dispersion bands with $N/5 = 8$ frequencies in each band.

Let us analyze how the natural frequencies of the ring vary with β. Let us consider the top dispersion band of the $p = 4$ and $p = 5$ lattices. These two lattices correspond to $\beta = 0$ and 1, respectively. At these two β values, all modes lie on the dispersion bands and the bands are separated by bandgaps for both the lattices. The number of frequencies changes from 10 to 8 as $10 - 8 = 2$ modes go to the second band (from the top) in the $p = 5$ lattice. There are 8 modes in the second band for $p = 5$ lattice, 6 modes go from the second band

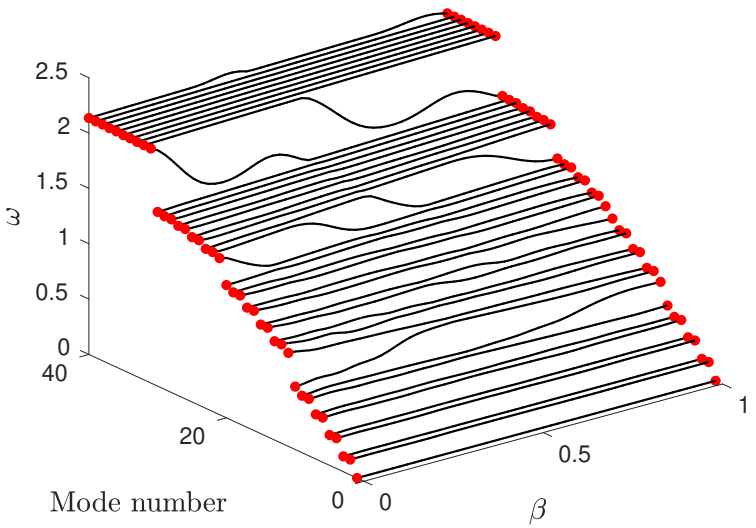

FIG. 7: Change in natural frequency of each mode with parameter β showing a spectral flow across the bandgaps. A number of modes traverse the gap to satisfy the requirement of equal number of modes in each dispersion branch at $\beta = 0$ and 1.

along with 2 modes from the top band at $\beta = 0$. Using similar counting arguments, we can determine how the 10 modes in each of the 4 branches of the $p = 4$ lattice get distributed into the 5 branches of the $p = 5$ lattice.

The key observation is that a number of modes flow across the bands as β varies from 0 to 1 to satisfy the requirement of $N/5 = 8$ and $N/4 = 10$ modes in each dispersion branch in the $p = 5$ and $p = 4$ lattice, respectively. This flow of natural frequencies, or spectral flow, arises solely to satisfy the topological constraint of the number of modes in each dispersion branch. For $\beta = 0$, there are 10 modes in each of the 4 bulk bands and for $\beta = 1$, there are 8 modes in each of the 5 bulk bands. The key topological argument is the following: as we vary β smoothly in $[0, 1]$, the only way to have a change in the number of modes in the top bulk band change from 10 to 8 is if $10 - 8 = 2$ modes migrate down to another bulk band. Thus, two modes traverse the bandgap as β is varied in $[0, 1]$ and these modes are labeled as topologically protected modes. This migration of modes is independent of the functional form of $p(\beta)$ in $[4, 5]$, with the only requirement being continuity. It is also independent of the specific functional form of k_m in Eqn. (12). Indeed, any functional form of k_m that gives distinct values 4 (or 5) distinct values of spring stiffness and leads to 4 (or 5) distinct dispersion bands should also exhibit such spectral flow.

In summary, we saw how modifying the parameter β smoothly from 0 to 1 leads to a spectral flow between the bandgaps. This hypothetical example of a lattice embedded on a ring shows the simplest realization of modes arising to satisfy the topological constraint of N/p modes in each dispersion branch. The ring shaped lattice in this hypothetical example can be extended to real structures where there is an interface or boundary between distinct lattice types. The mode shapes corresponding to the modes traversing the bandgap will be localized at such interfaces and boundaries. Indeed, such modes cannot be bulk modes since their natural frequency is in the bandgap. Since they have a topological origin, such modes cannot be removed in the presence of a wide class of defects or imperfections.

In the subsequent examples in this section, we will see how a similar spectral flow between bulk bands arises at a boundary of a lattice or at an interface between two lattices. The bulk dispersion surfaces of these lattices are characterized by topological invariants and such interface/boundary modes arise when they have different/non-zero topological invariants.

B. Localized modes in beams

Our next example shows how a spectral flow similar to that discussed in Sec. IV A arises in an elastic beam with ground springs. Figure 8 displays the schematic of the considered system, where the ground springs are located at a distance specified by a parameter θ. There are circles of radius r with centers located distance a apart, with $r < a$. The n-th ground spring location is obtained by projecting a point at an angle $n\theta$ from the circle to the beam. Specifically, this location is $x_n = na + r\sin(2\pi n\theta)$ and the periodicity of the resulting lattice pattern thus depends on θ. If θ is a rational number, for example p/q, where p and q are co-prime integers, then a unit cell has q springs. On the other hand, if θ is an irrational number, then there is no repetitive unit cell and the resulting structure is quasiperiodic.

The plane wave expansion method discussed in Sec. III A may be used to determine the natural frequencies of the beam structures considered here. The basis functions in Eqn. (4) running over a single index m are a valid choice, as they are periodic over a unit cell[69]. Figure 9a displays the natural frequencies of a finite beam (red curves) overlaid on the corresponding frequencies for an infinite beam. It shows how the frequencies change with the parameter θ. Note that each vertical slice (constant θ line) is a different lattice. A homogeneous beam (without ground springs) has an infinite number of natural frequencies

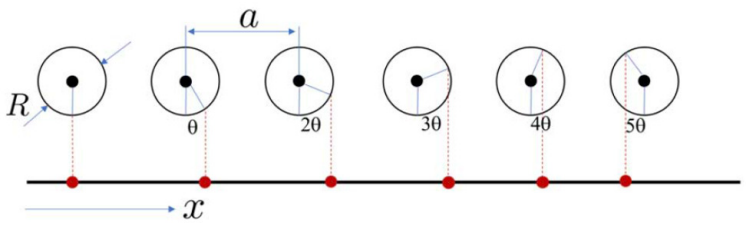

FIG. 8: Schematic of procedure to determine the location of each ground spring by projecting from a circle. Varying the parameter θ gives a family of periodic (quasiperiodic) structures for rational (irrational) θ[69].

without an upper bound and its dispersion relation is

$$\omega = \sqrt{\frac{EI}{\rho A}}\kappa^2.$$

Here κ is the wavenumber and E, I, ρ and A denote the Young's modulus, area moment of inertia, density and cross-section area of the beam. Let us first consider the $\theta = 0$ beam structure. Having a periodic arrangement of ground springs introduces a length scale, the distance a between adjacent ground springs. This length scale of the resulting unit cell introduces Bragg scattering bandgaps in the dispersion surface. For a finite beam with N ground springs and simply supported boundary conditions, there are N modes in this first band, i.e., below the first bandgap. This observation follows from similar arguments as the discrete lattice embedded on a ring that was considered in Sec. IV A.

Let us restrict attention to this first dispersion band at $\theta = 0$. As the parameter θ is varied in the set $[0, 1]$, this band splits into a number of smaller bands with bandgaps between them. The red curves corresponding to the finite beam fall within the bulk bands as θ takes values in the set $\{p/N : p = 1, 2, \ldots N\}$. For these values of θ, one can double the length L of the beam and set $u(L + x) = -u(L - x)$ and check by direct substitution that this displacement field will be an eigenmode of the doubled beam. This transformation now allows us to identify the mode shapes with that of a corresponding beam shaped in the form of a ring, i.e., without a boundary. Using similar arguments for the beam as in Sec. IV A, we arrive at this set $\{p/N : p = 1, 2, \ldots N\}$ of θ values. In addition, we observe spectral flow between the bulk bands as θ changes between these discrete values.

We thus see features similar to that observed in the hypothetical ring lattice in Sec. IV A in the elastic beam. Furthermore, the number of modes that traverse from one band to the

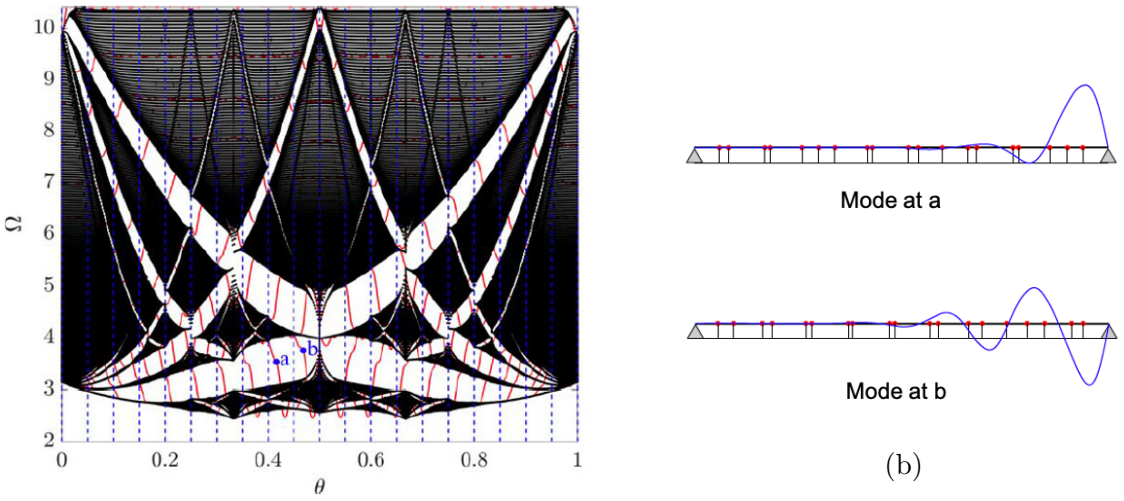

(a) (b)

FIG. 9: (a) Frequencies of a finite beam with 20 ground springs (red curves) superimposed on infinite beam frequencies (black curves) for a family of lattices. Each θ is a distinct structure. Spectral flow between bulk bands (contiguous black curves) arises. (b) Mode shapes of two localized modes at points a and b in (a)[69].

other can also be determined using similar counting arguments. For example, let us consider two beam lattices, one with $\theta = 1/5$ and the other with $\theta = 1/4$. The first band at $\theta = 0$ splits into 5 and 4 dispersion bands, respectively. The first $N = 20$ natural frequencies of the finite lattice are distributed equally in these dispersion bands. As θ varies between these two values, we observe a spectral flow between the various bands similar to the discrete lattice case. In particular, one mode flows from the bottom band of the $\theta = 1/5$ beam lattice to the second band of the $\theta = 1/4$ lattice to satisfy the constraint of specific number of modes in each band.

Having demonstrated how a similar spectral flow arises in an architected beam, let us examine the mode shape of this mode. Figure 9b displays two representative mode shapes, for modes in the bandgap marked as (a) and (b) in Fig. 9a. The modes are localized at the right boundary of the beam and their displacement amplitude decreases rapidly with distance from this end. Note that there are $N = 20$ such modes spanning this large bandgap - having modes marked (a) and (b) - as θ varies from 0 to 1. This number N is equal to the number of ground springs in the finite beam[69]. For practical applications, it is more desirable to have a system or structure where the number of localized modes in a bandgap

is independent of the system size. The next example achieves this and its topological modes are independent of the number of unit cells in the lattice structure.

C. Topological elastic pumping of localized modes

In the last section, we saw how to achieve localized modes at the boundary of an elastic beam. Let us now study an example of a structure that can support transport of elastic energy by exploiting such topological modes. This example is inspired by the Thouless charge pump in quantum mechanics[72,73]. We start by considering a mass-spring chain whose stiffness k_n of the n-th spring is

$$k_n = 1 + \alpha \cos\left(\frac{2\pi n}{3} + \phi\right). \tag{13}$$

Here $\alpha < 1$ and ϕ takes values in the set $[0, 2\pi]$. There are 3 masses in each unit cell and hence the lattice has 3 dispersion surfaces.

Figure 10a displays the dispersion surfaces for a family of lattices as ϕ varies from 0 to 2π and $\alpha = 0.6$. The bandgaps do not close for small α. Now, let us consider a finite chain of 61 masses. This chain has $N = 20$ unit cells and an extra mass is added so that we get a *commensurate lattice*, one whose modes can be identified with modes in the corresponding infinite chain for $\phi = 0$. Figure 10b displays how the natural frequencies change with ϕ for this finite chain. Note that there is a mode that spans each bandgap as it flows from one bulk band to another and then back again. The solid and dashed lines in this bandgap indicate a mode localized at the left and right boundary, respectively. Figure 10c displays the mode shape of the mode spanning the first bandgap, showing how it transitions from one edge to another in the finite chain.

The origin of this spectral flow is also topological as the number of modes n_i in each bulk band changes as ϕ changes by π. For this considered lattice, all the modes lie on dispersion surfaces at $\phi = 0$ and $\phi = \pi$. The total number of modes is $3N + 1$ and they are distributed differently in each of the bulk bands for the two lattices $\phi = 0$ and $\phi = \pi$. The number of modes n_i can be determined directly by explicit calculations. The lattices at $\phi = 0$ and $\phi = \pi$ are illustrated in Fig. 11a. Note that the unit cells of these two lattices are translated copies of each other but the key point is that the location of the lowest spring stiffness is different. This difference leads to differences at the two ends of a finite chain and their

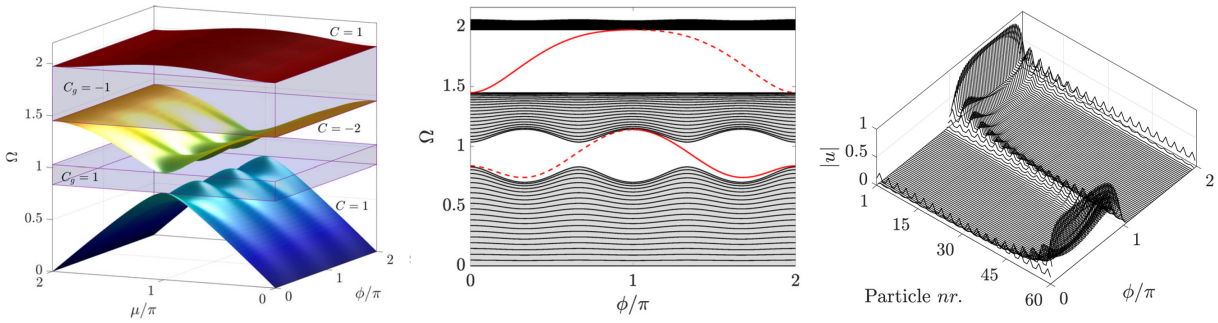

(a) (b) (c)

FIG. 10: (a) Dispersion surfaces of a family of lattices as a function of ϕ showing 2 bandgaps between the bulk bands, along with the Chern number. (b) Natural frequencies of a finite chain of $N = 61$ masses showing a spectral flow across the bandgap as ϕ varies. Dashed (solid) curves indicate the mode is localized on the left/right boundary. (c) Displacement magnitudfe of the localized mode in the second (higher) bandgap showing the transition from right to left boundary[74]. (Reproduced with permission from Phys. Rev. Lett. 123, 034301 (2019). Copyright 2019 American Physical Society.)

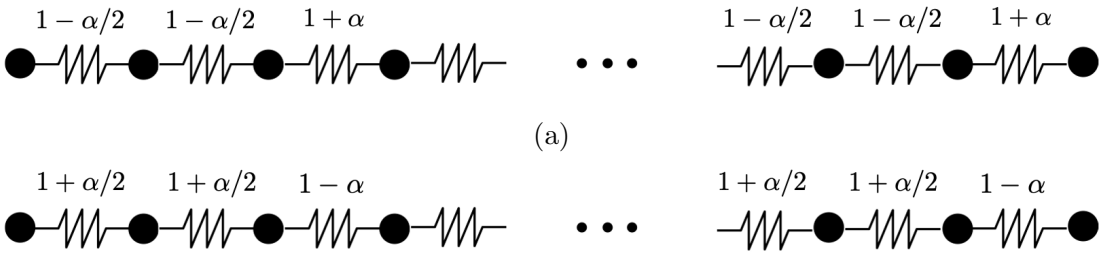

(a)

(b)

FIG. 11: The finite lattice at (a) $\phi = 0$ and (b)$\phi = \pi$ has distinct stiffness distribution. The number of frequencies lying on the first and third dispersion branches are different for $\phi = 0$ and π. This difference implies a spectral flow in the bandgap as ϕ varies in $[0, \pi]$.

resulting natural frequencies. A direct calculation yields $n_1 = N + 1$, $n_2 = n_3 = N$ for the $\phi = 0$ lattice and $n_1 = n_2 = N$, $n_3 = N + 1$. The only way to have this change in the discrete number of modes between the two lattices is to have a spectral flow of a mode from the first band to the second and another mode from the second to the third band as ϕ varies from 0 to π.

The lattice above shows a specific example where varying a single parameter results in a

spectral flow of a localized mode across the bandgap. It leads to the natural question: what class of lattices exhibit such spectral flow of a localized mode across a bandgap? The answer to this question is related to the Chern number, a topological invariant of a vector field over a manifold[75]. In particular, the eigenvectors that are mode shapes in each band constitute a vector field. If there are n degrees of freedom in a unit cell, then each eigenvector has n components. These n components are complex numbers, with the additional property that if $\boldsymbol{u}$ is an eigenvector, then $\beta\boldsymbol{u}$ is also an eigenvector for any nonzero complex number β. Let us consider a family of lattices whose properties vary smoothly with a parameter ϕ such that the dynamic matrix is a periodic function of ϕ, i.e., $\boldsymbol{D}(\phi) = \boldsymbol{D}(\phi + 2\pi)$. Let us also define $\Omega = [0, 2\pi] \times [0, 2\pi]$ as the domain in the wavenumber μ and parameter ϕ plane. Dispersion analysis of each lattice in this family gives n eigenvectors for each ϕ and wavenumber μ. There are n dispersion surfaces and hence n vector fields of the corresponding eigenvectors in Ω. The Chern number of a band measures a topological property of the vector field comprised of its eigenvectors. It is given by

$$C = \frac{1}{2\pi i} \int_{\Omega} [\nabla \times (\boldsymbol{u}^* \cdot \nabla \boldsymbol{u})]_3 \, d\Omega.$$

Note that the eigenvectors $\boldsymbol{u}$ of a dispersion band is periodic in this plane with period 2π along each axes. $\boldsymbol{u}$ is periodic in μ due to the periodicity of the Brillouin zone.

The reader may refer to several excellent sources for a detailed derivation and mathematical properties of the Chern number[75–77]. Here we give an intuitive introduction to the physical meaning of this quantity that is relevant to the present topic. The Chern number is equal to the number of singularities in the phase of the vector field in Ω. To see how such a singularity arises and its relation to localized modes at a boundary, let us consider a dispersion surface of a lattice with n degrees of freedom per unit cell. The eigenvector at each (μ, ϕ) can be expressed as a unit vector in $\mathbb{C}^n$, i.e., an n-component vector over the complex number field.

Let us determine how $\boldsymbol{u}$ and its derivatives change as we move along a path in Ω. Recalling that $\beta\boldsymbol{u}$ is also an eigenvector for any complex number β, we can still write down a phase independently for each eigenvector, i.e., each member in the set $\{e^{i\theta}\boldsymbol{u}\}$ with $\|\boldsymbol{u}\| = 1$ is also an eigenvector. To meaningfully compare $\boldsymbol{u}$ at two distinct points in the (μ, ϕ) plane, we need to fix a gauge - a generalized coordinate system specifying θ. Otherwise the phase θ at any two distinct points can make the individual components arbitrary. In particular, we

need to make a choice for the phase $\theta(\mu, \phi)$ as a function of μ and ϕ. By Stokes theorem, the Chern number for the vector field $\boldsymbol{u}(\mu, \phi)$ in the domain Ω becomes

$$C = \int_{\partial\Omega} [\boldsymbol{n} \times (\boldsymbol{u}^* \cdot \nabla \boldsymbol{u})]_3 \, d\partial\Omega. \tag{14}$$

Here $\boldsymbol{n}$ is the unit outward normal from Ω at a point on the boundary $\partial\Omega$. If there is a smooth choice possible, then the Chern number becomes zero due to periodicity of $\boldsymbol{u}(\mu, \phi)$ in Ω. If no such smooth choice of a phase field is possible, then this results in a discontinuity in $\theta(\mu, \phi)$. In particular, it can be shown that[74]

$$\boldsymbol{u}(\phi = 2\pi, \mu) = e^{is\mu} \boldsymbol{u}(\phi = 0, \mu).$$

Here s is an integer. Substituting the above relation into Eqn. (14) gives $C = s$. The key message is that C is non-zero only when there is a discontinuity in the phase field θ.

Now, let us consider a family of finite lattices generated by varying ϕ from 0 to 2π. If the Chern number of a band is $C = s \neq 0$, then there are s modes traversing the bandgap above it as ϕ changes in $[0, 2\pi]$. A simple way to understand this spectral flow is to note that a zero Chern number implies that the modes in the finite lattice can be smoothly deformed as ϕ varies in $[0, 2\pi]$. Similarly, a nonzero Chern number implies that all modes cannot be smoothly deformed or mapped as we vary ϕ. Hence the only possibility is that some modes lie in multiple bands when $\phi = 0$ and π. As ϕ varies in $[0, 2\pi]$, these modes traverse the bandgap and this traversal is the observed spectral flow between bulk bands. The net number of such modes equals the number of singularities in the phase field, i.e., the absolute value of the Chern number. The sign of the Chern number indicates whether the modes traverse from or to the band as ϕ varies in $[0, \pi]$. Hence any lattice whose dispersion band has a non-zero Chern number s in the (μ, ϕ) supports a net number $|s|$ of modes traversing the bandgap to the bulk band above it.

Let us see how this family of localized modes can be used to achieve transport of elastic waves. Figure 12 displays an array of beams coupled with continuous distributed springs along their length. The key idea is to have a family of lattices with varying ϕ so that the localized mode moves from one boundary to another. The springs have stiffness analogous to Eqn. (12) with the ϕ varying along the length of the chain. Hence each segment of the distributed spring at a distance z along the length is equivalent to a discrete elastic chain at a value $\phi(z)$. If ϕ is varied from $\pi/3$ to $2\pi/3$, we note that the localized mode shifts

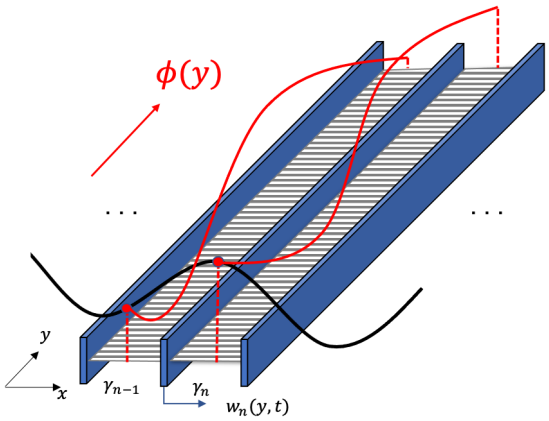

FIG. 12: Schematic of an array of beams coupled with distributed springs whose stiffness is given by Eqn. (13). Along the beam, ϕ varies from $\pi/3$ to $2\pi/3$ so that the localized mode in this chain of distributed springs traverses from left to right boundary.

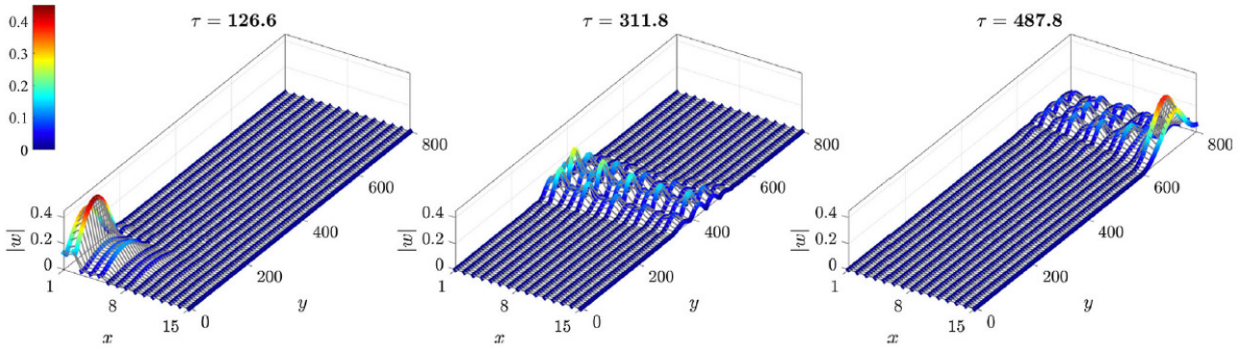

FIG. 13: Snapshots of beam displacements at 3 distinct time instants showing how the wave transitions from a left localized to a bulk wave to finally a right localized wave[74]. (Reproduced with permission from Phys. Rev. Lett. 123, 034301 (2019). Copyright 2019 American Physical Society.)

from the right to the left boundary, as illustrated by the distinct time snapshots of the displacement field in Fig. 13. This transport happens when the structure is subjected to a dynamic excitation with frequency in the first bandgap. An experimental demonstration of this wave propagation was achieved in[78] in a plate whose bending stiffness is modulated by varying its thickness. This example shows how to achieve energy transport from one corner to another in an elastic structure. The next example illustrates wave transport between any two points on the boundary of a $2D$ mechanical lattice.

D. Mechanical spin Hall effect

The mechanical analogue of the quantum Hall effect allows for one way transport along the boundaries of a structure. It is inspired by works in quantum mechanics starting with the Haldane model [79], where electrons move in one direction along the edges of a $2D$ electron gas. In recent years, several works have achieved mechanical analogues of this effect in both periodic and random media. The basic idea is the same as was discussed for localized modes in the family of lattices in Sec. IV C. Instead of a $1D$ family of lattices, we have a $2D$ lattice with the wave vector along the direction tangential to the boundary playing the role of ϕ. Such modes are achieved in lattices whose dispersion bands have a nonzero Chern number. It requires using springs with imaginary stiffness that break time reversal symmetry and is realized using active mechanical components like rotating gyroscopes[22,23].

To illustrate this concept, let us study the hexagonal lattice in Fig. 14a. It consists of rotating gyroscopes attached to the masses at each lattice site. There are two dispersion bands for this lattice with Chern numbers +1 and -1 for the lower and upper bands, respectively. These numbers are evaluated by considering the vector field of mode shapes for each band in the two-dimensional wave-vector domain $\boldsymbol{\kappa} = (\kappa_x, \kappa_y)$.

To demonstrate the existence of edge modes in such lattices, a common technique is to consider the dispersion of a single strip of finite width shown in Fig. 14b. Periodic boundary conditions are imposed on the long inclined boundaries and the lattice is thus one dimensional with wavenumber equal to the wave-vector component κ_x. Figure 14b displays the dispersion curves for such a finite strip. Most of the modes of the strip lie in the frequency range of the bulk dispersion surfaces obtained with a single unit cell. In addition, two modes traverse the bandgap as κ_x varies from 0 to 2π. Their corresponding mode shapes are localized on each boundary.

The reason for this spectral flow is the same as the concept discussed in Sec. IV C. A non-zero Chern number implies the existence of a spectral flow across a bandgap to satisfy the condition that a singularity exists in the phase field. This lattice thus supports edge modes localized at the boundary for all frequencies in the bandgap. In addition, they have a positive (negative) group velocity on the top (bottom) surface. Indeed, recall that the group velocity is the gradient of the frequency with respect to the wave vector[80]. Hence, these modes propagate only one way along each boundary and in effect, traverse clockwise

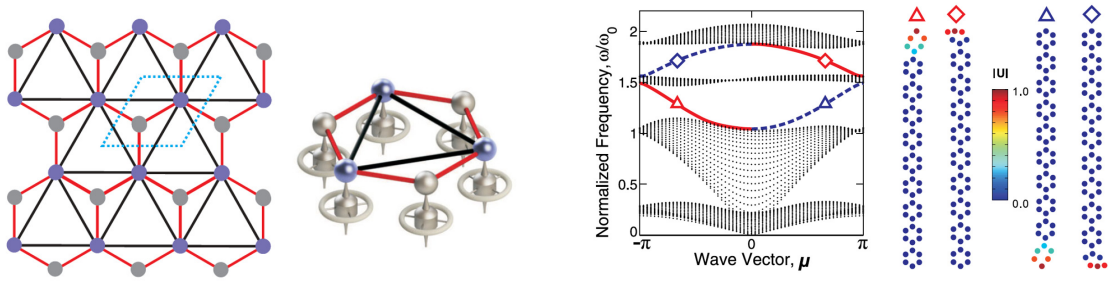

(a) (b)

FIG. 14: Elastic lattice supporting chiral edge modes. (a) Hexagonal lattice with rotating gyroscopes at each node. (b) Dispersion curves for a strip as a unit cell showing one way modes in the bandgap. The red (blue) modes are localized at the top (bottom) surface and traverse counter-clockwise around the boundary[23]. (Reproduced with permission from Phys. Rev. Lett. 115, 104302 (2015). Copyright 2015 American Physical Society.)

around a finite lattice.

Note that there are no continuous analogues of this effect in conventional elastic media. This hexagonal lattice of Haldane was extended to derive another class of topological edge modes called helical modes and the associated phenomena is called the quantum spin Hall effect. It essentially consists of two copies of the Haldane model lattice and the total system preserves time reversal symmetry. The quantum Hamiltonian $\boldsymbol{H}$, which is the analogue of the dynamic stiffness matrix $\boldsymbol{M}^{-1}\boldsymbol{K}$ of a mechanical system, has the form

$$\boldsymbol{H}(\boldsymbol{\kappa}) = \begin{pmatrix} h(\boldsymbol{\kappa}) & 0 \\ 0 & -h^*(\boldsymbol{\kappa}) \end{pmatrix} \tag{15}$$

Figure 15 displays examples of discrete mechanical lattices that support such helical edge modes. The advantage of this class of modes is that they do not require active components and can be realized in conventional linear elastic media. The key idea is that two copies of any lattice whose dispersion bands have non-zero Chern number can be used to construct a lattice that supports helical edge modes. The Chern number of each band in the combined assembly is zero. Susstrunk and Huber used this concept on a square Hofstadter lattice with 6 degrees of freedom per unit cell to achieve a mechanical analogue of this quantum spin Hall effect. They obtained the first experimental observation of helical modes in a mechanical system that has 2 copies of a square lattice with 6 degrees of freedom per unit

cell (Fig. 15a). The experimental setup consists of an array of interconnected pendulums and levers to mimic springs with positive and negative stiffness. Their key idea to handle the imaginary terms in $h(\boldsymbol{\kappa})$ was to use the unitary transformation

$$\boldsymbol{U} = \boldsymbol{I}_N \otimes \frac{1}{\sqrt{2}} \begin{pmatrix} 1 & i \\ 1 & -i \end{pmatrix} \tag{16}$$

to convert the Hamiltonian to a matrix with only real terms. Here N is the number of unit cells of a finite lattice. The dynamic stiffness matrix $\boldsymbol{D} = \boldsymbol{U}^\dagger \boldsymbol{H} \boldsymbol{U}$ has the same eigenvalue spectrum as $\boldsymbol{H}$. In addition, if a wavefunction $\boldsymbol{u}$ is localized in the quantum case, its corresponding mechanical mode shape $\boldsymbol{U}\boldsymbol{u}$ will also remain localized in the mechanical lattice. This preservation of localization is due to the block diagonal form of $\boldsymbol{U}$. This form ensures that the mode shape (eigenvector of $\boldsymbol{D}$) components in each unit cell can be expressed as a linear function of the corresponding eigenvector components of $\boldsymbol{H}$ in the same unit cell.

Let us discuss in detail the design constructed by one of the authors of this tutorial in[25]. Figure 15b displays a unit cell consisting of rotating disks connected by bars. Each disk has one degree of freedom and can rotate in its plane. Our starting point is the Hamiltonian used by Kane and Mele[81], that supports helical edge modes at the boundary of a hexagonal lattice. Their model has two copies of hexagonal lattice and each unit cell thus has 4 degrees of freedom. These degrees of freedom are coupled through real and imaginary interaction terms and these couplings are analogous to springs connecting masses in a mechanical system. However, in a discrete mechanical system, it is desirable that all spring stiffness values are real. To achieve this condition of real coupling terms, we apply the transformation $\boldsymbol{U}$ in Eqn. (16) to get a stiffness matrix with all real terms. In particular, after applying Bloch periodicity condition, the stiffness matrix for the hexagonal lattice unit cell takes the form

$$\boldsymbol{K} = \begin{pmatrix} \boldsymbol{K}_1 & \boldsymbol{K}_2 \\ \boldsymbol{K}_2^* & \boldsymbol{K}_1 \end{pmatrix},$$

with

$$\boldsymbol{K}_1 = (3k + 6\lambda)\boldsymbol{I}_2 - k(1 + e^{i\boldsymbol{\kappa}\cdot\boldsymbol{a}_1} + + e^{i\boldsymbol{\kappa}\cdot\boldsymbol{a}_2})\sigma_x,$$
$$\boldsymbol{K}_2 = \lambda \left(e^{i\boldsymbol{\kappa}\cdot\boldsymbol{a}_1} - e^{i\boldsymbol{\kappa}\cdot\boldsymbol{a}_1} + e^{-i\boldsymbol{\kappa}\cdot\boldsymbol{a}_2} - e^{i\boldsymbol{\kappa}\cdot\boldsymbol{a}_2} + e^{-i\boldsymbol{\kappa}\cdot(\boldsymbol{a}_1 - \boldsymbol{a}_2)} - e^{i\boldsymbol{\kappa}\cdot(\boldsymbol{a}_1 - \boldsymbol{a}_2)} \right) \sigma_z.$$

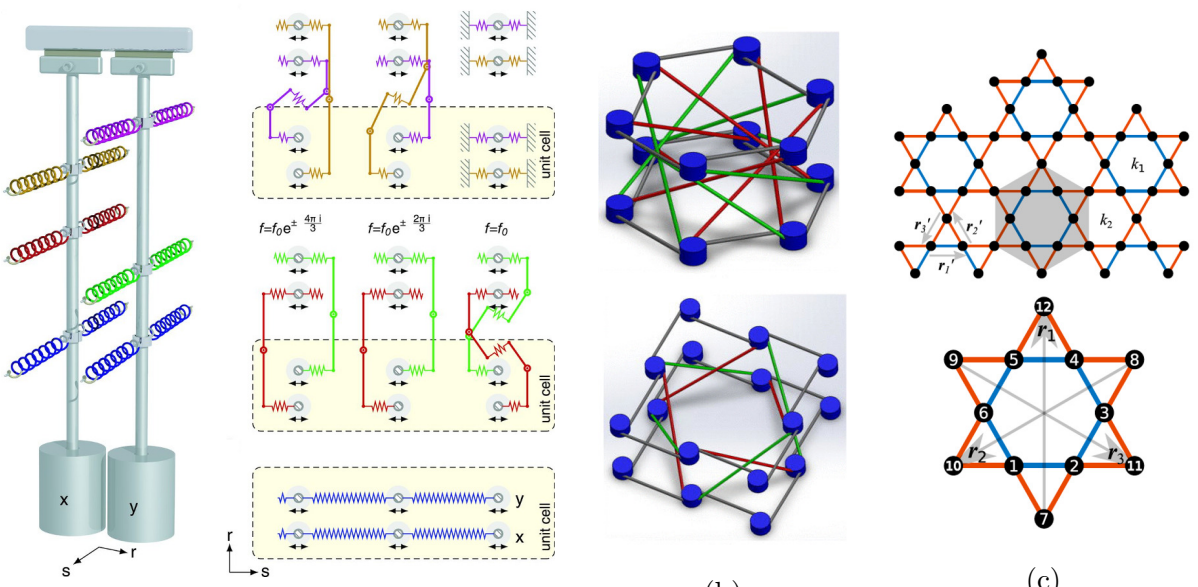

FIG. 15: Examples of discrete mechanical lattices that support helical edge modes. (a) Pendulums with springs[24], (b) rotating disks[25] and (c) spring mass lattice[82]. (Reproduced with permission from Science 349, 47-50 (2015), J. Appl. Phys. 995 119, 084305 (2016) and Phys. Rev. B 98, 094302 (2018). Copyright 2015 Amer. Assoc. Adv. Science and 2018 American Physical Society.)

Here σ_x and σ_z are Pauli matrices and k, $\pm\lambda$ are the stiffness values of the intra- and inter-layer coupling springs, respectively. Figure 15b (top) displays a schematic of a hexagon of the resulting lattice along with the connectivity between the disks.

Figure 16a displays the dispersion diagram for the lattice with $\lambda = 0$, i.e., no interlayer coupling springs. The dispersion diagram is projected onto the $\kappa_y = 0$ plane. There is no bandgap and the two dispersion surfaces touch. Figure 16b displays the corresponding dispersion diagram of a unit cell with interlayer coupling $\lambda = 0.2$ showing a bandgap now opens up. To see the presence of topological modes at a boundary, we again examine the dispersion curves of a lattice that is finite in one direction and infinite in another, similar to the lattice in Fig. 14b. They are illustrated in Fig. 16c and have two modes spanning the bandgap in addition to the bulk bands seen in Fig. 16b. The difference between these two dispersion curves (Figs. 16b, 16c) is the effect of a finite boundary. Indeed, the mode shapes corresponding to the modes in the bandgap are localized at a boundary. Note how

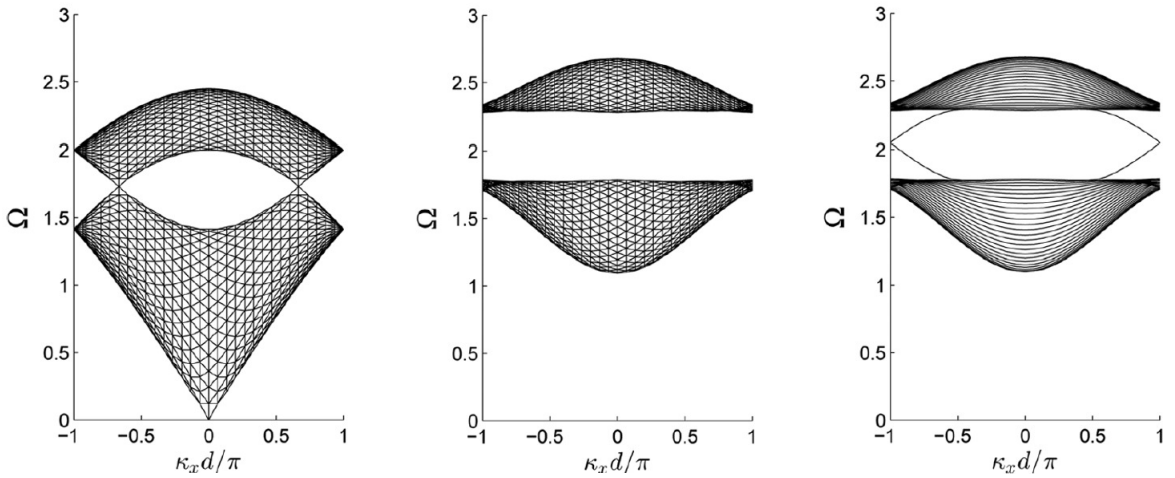

FIG. 16: Dispersion of a unit cell (a) without and (b) with interlayer coupling, showing how Dirac points break to generate a bandgap. (c) Dispersion of a finite strip showing modes spanning the bandgap[25]. (Reproduced from J. Appl. Phys., 119, 084305 (2016), with the permission of AIP Publishing.)

they span the entire bandgap. In contrast to the chiral edge modes in Fig. 14b, there are two modes with opposite group velocities traversing the bandgap.

Let us now see the transient behavior of a finite lattice comprised of these unit cells subjected to narrow band excitation (like a tone burst) in the bandgap frequency. Figure 17 displays the snapshots of displacement field at various time instants for each of these waves. They are localized at the boundary and their magnitude decays rapidly away from it. These discrete models serve to illustrate the key concept behind such waves in mechanical lattices, but they may not extend straightforwardly to continuous elastic media. In Sec. V B, we will show an example of helical waves in architected plates whose design is guided by symmetry considerations. Before that, let us turn attention to studying another class of topological modes: valley modes, that are supported at the interface between two hexagonal lattice.

E. Mechanical valley Hall effect

Valley modes are a class of topological modes that arise due to symmetry properties of Dirac cones in hexagonal lattices[57,83–86]. $2D$ periodic lattices with specific symmetry

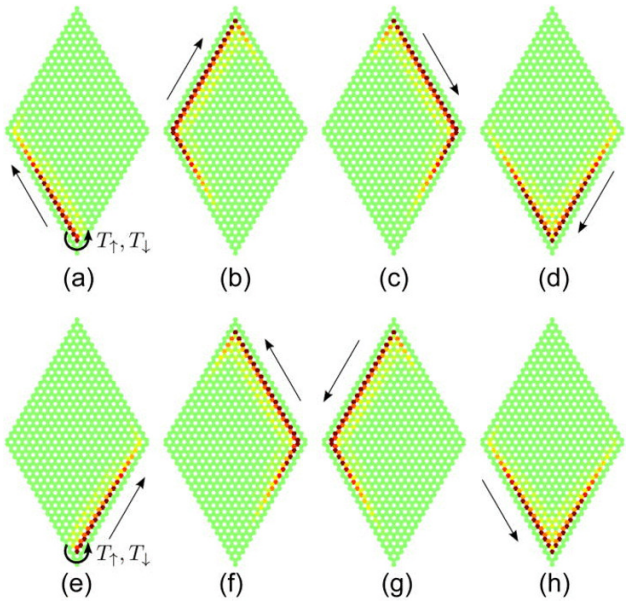

FIG. 17: Snapshots of displacement field at various time instants. Wave propagates clockwise (a-d) or counter-clockwise (e-h) depending on which mode is excited[25]. (Reproduced from J. Appl. Phys., 119, 084305 (2016), with the permission of AIP Publishing.)

properties exhibit singular features called Dirac cones in their dispersion surfaces. To see an example of how they arise, let us consider the hexagonal discrete mass-spring lattice shown in Fig. 18a. Each mass has one degree of freedom and can move out of plane. Each unit cell has 2 sub-lattice sites, indexed by a, b, and thus 2 degrees of freedom . The governing equations for a unit cell indexed p, q are given by

$$m_a \ddot{u}_{p,q,a} + k(u_{p,q,a} - u_{p,q,b}) + k(u_{p,q,a} - u_{p-1,q,b}) + k(u_{p,q,a} - u_{p,q-1,b}) = 0,$$
$$m_b \ddot{u}_{p,q,b} + k(u_{p,q,b} - u_{p,q,a}) + k(u_{p,q,b} - u_{p+1,q,a}) + k(u_{p,q,b} - u_{p,q+1,a}) = 0.$$

Figure 18b displays the two dispersion surfaces over the first Brillouin zone. They touch at the six high symmetry K points. In the vicinity of these points, the dispersion surface resembles a two cones whose apex touch and these points are called Dirac points. Figure 18c displays the dispersion surfaces along the path sketched at the base in Fig. 18b. Such Dirac cones are at the heart of unique physical properties of graphene[87]. The unique property of Dirac cones is that the mode density at that frequency is very low but the group velocity is finite, equal to the gradient of dispersion dispersion surface near the cone tip.

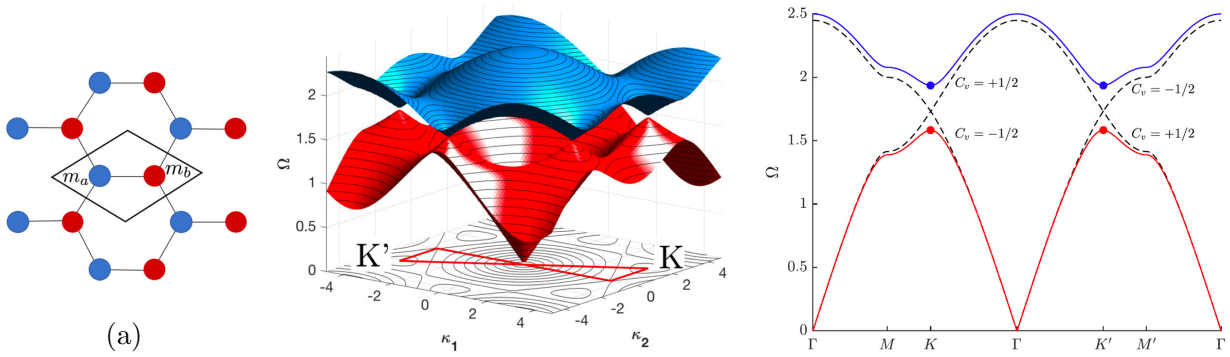

FIG. 18: (a) Hexagonal lattice schematic with unit cell. (b) Dispersion surfaces when $m_a = m_b$ showing Dirac cones at the K points. (c) Dispersion curves over a path through the high symmetry points for the case $m_a \neq m_b$ (solid curves) and $m_a = m_b$ (dashed curves). The valley Chern numbers C_v for each band at the K points are indicated[88]. (Reproduced with permission from Phys. Rev. B 96, 134307 (2017). Copyright 2017 American Physical Society.)

Let us see what happens if we break inversion symmetry by making the masses at the two sub-lattice sites different. The broken inversion symmetry is about the unit cell center, i.e., the structure is different under the transformation $\boldsymbol{x} \to -\boldsymbol{x}$. The degeneracy of the two modes at the K points break and a bandgap opens up. Again, similar to the case of Sec. IV A and Sec. IV D, the vector field associated with the bands have topological properties that lead to the existence of localized modes spanning the bandgap frequencies. In contrast to the earlier cases, where such modes are localized at the domain boundary, these modes are localized at the interface between two lattices that are inverted copies of each other.

Let us start by considering the lattice shown in Fig. 19. The strip is infinite along the x-direction but finite along the y-direction. The boundary masses at both ends are fixed. The masses at the two sub-lattice sites (red and white circles) are different. There is an interface at the center of the strip and the unit cells on both sides are inverted copies of each other. This lattice is periodic along the x-direction and the dashed parallelogram shows a unit cell of this lattice.

Let us analyze the dispersion behavior of this finite strip lattice. Let the light and heavy mass values be $m_1 = 1$ and $m_2 = 2$, respectively. There are two types of lattices depending

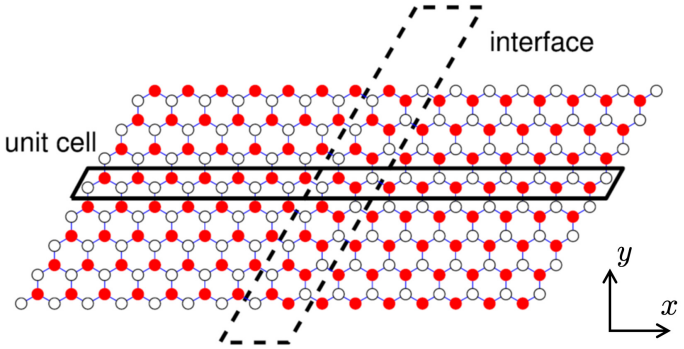

FIG. 19: Schematic of a lattice periodic along horizontal edges and finite along tilted edges. Red and white circles have distinct masses. The interface separates two parts that are inverted copies of each other[57].

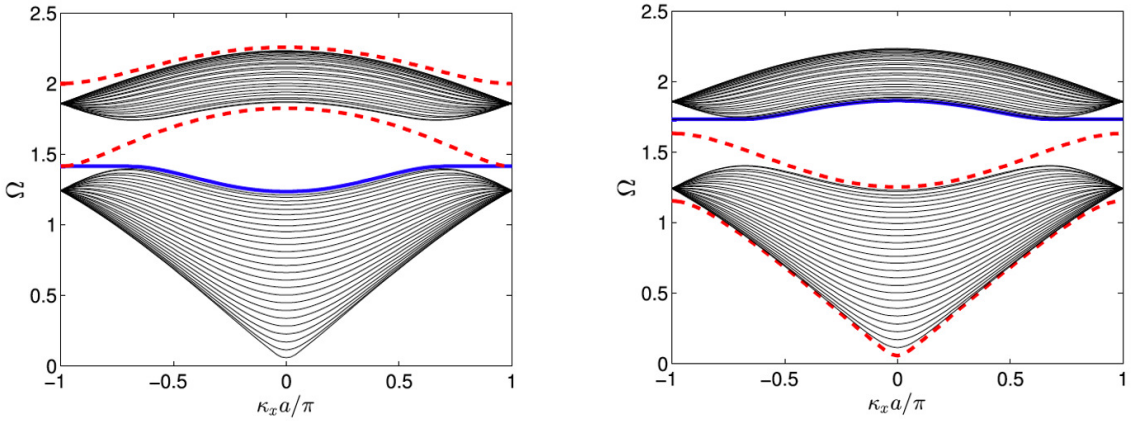

FIG. 20: Dispersion diagrams of a finite strip with an interface having adjacent (a) light and (b) heavy masses. Mode shapes of the dashed red and solid blue curves are localized at the interface and boundary, respectively[57].

on whether there are adjacent light or heavy masses at the interfaces. Figure 20 displays the dispersion curves for both cases. The dashed lines indicate modes localized at the interface while the solid blue lines are modes localized at the boundary. The remaining two contiguous sets of curves correspond to modes spanning the entire unit cell, i.e., bulk modes. The key observation is that the mode shape and frequency-wavenumber relation of the localized mode can change depending on the interface type, but there is a mode in the bandgap for both cases.

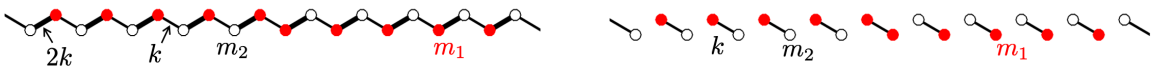

(a) (b)

FIG. 21: Schematic of finite strip lattice with interface at the high symmetry points (a) $\kappa_x = 0$ and (b) $\kappa_x = \pi/a$ after applying Bloch periodicity. The two configurations have distinct number of frequencies lying in each bulk band, implying a mode traverses the bandgap as κ_x varies in $[0, \pi/a]$.

There are two different approaches to understand the existence of these localized modes at such interfaces, similar to the two distinct approaches presented in Sec. IV C. The first approach analyzes the behavior at distinct high symmetry points to infer the existence of a spectral flow in the bandgap, while the second approach uses topological invariants to infer localized modes in the bandgap.

In the first approach, let us consider the dynamic behavior of the lattice at wavenumbers $\kappa_x = 0$ and $\kappa_x = \pi/a$. Here a is the unit cell length. Using Bloch periodicity conditions, we see that all unit cells have identical displacement fields at $\kappa_x = 0$, while adjacent unit cells have displacement field of opposite sign at $\kappa_x = \pi/a$. These relations lead to the unit cell transforming into the lattices shown in Fig. 21a and 21b for $\kappa_x = 0$ and π/a, respectively. Thick lines indicate that the stiffness value is $k = 2$. These transformed lattices are obtained by using the above displacement field relations at these wavenumbers and the connectivity of the hexagonal lattice. Similar to the case of topological pumping in Sec. IV C, direct calculations show that the frequency distribution in each of the bulk bands is different at these two wavenumbers. The difference in frequency arises for both kinds of interfaces: adjacent light masses and adjacent heavy masses, and it manifests as a spectral flow between the bulk bands. Again, there is a topological invariant that captures this difference in mode distribution and predicts the existence of localized modes. This invariant is the valley Chern number and it is equal to the integral of the Berry curvature in the vicinity of the K-point. Detailed derivations of this invariant are presented in[57]. It should be noted that having distinct masses that break inversion symmetry is one possible way to achieve topological bandgaps. Recent works[89] have demonstrated band inversion in spring mass models that preserve inversion symmetry.

V. EDGE MODES IN ELASTIC PLATES

Having discussed various kinds of topological modes localized at interfaces and boundaries in architected beams and discrete $2D$ mechanical lattices, let us now see examples of how these concepts can be extended to architected plates. We will consider 3 examples in increasing order of structural complexity. The first one supports valley Hall modes in thin plates using zero order bending or A_0 Lamb waves. The second example achieves helical edge waves using the hybridization of multiple higher order Lamb wave modes in a plate with complex-shaped blind and through holes. The final example extends this plate design to support both helical and valley modes, along with splitting or redirection of a wave at a junction depending on its polarization.

A. Elastic valley Hall modes

In Sec. IV E, we discussed the discrete mechanical analogue of the quantum valley Hall effect in lattices that have C_3 rotational symmetry but broken inversion symmetry. The key idea is that localized modes arise at the interface of two such lattices that are inverted copies of each other. Let us see how to extend this discrete concept to continuous elastic media.

Architected thin plates supporting Lamb waves provide a way to realize a wide class of waves that are continuous analogues of $2D$ discrete mechanical lattices. Examples include hexagonal and Kagome lattices in[88,90,91]. The common aspect in these designs is that they all satisfy the aforementioned symmetry conditions for the discrete case. Let us discuss in detail the design in Fig. 22a. It consists of a thin plate with hexagon shaped holes drilled into it in a periodic arrangement. Masses are attached at nodal locations in a corresponding discrete hexagonal lattice. The masses attached at the two sub-lattice sites in the unit cell are different and this difference breaks inversion symmetry of the lattice.

Figure 22b displays the corresponding dispersion bands for a single unit cell. It is computed using finite element analysis and it shows a bandgap opening up due to the breaking of inversion symmetry at the K-point. Note that the bending modes that form a Dirac cone breaks to form a bandgap, but it is not a complete isolated bandgap as there are axial and in plane-shear modes that traverse this frequency range. However, due to their distinct mode shapes, when the bending mode is excited, a negligible fraction of energy is converted to

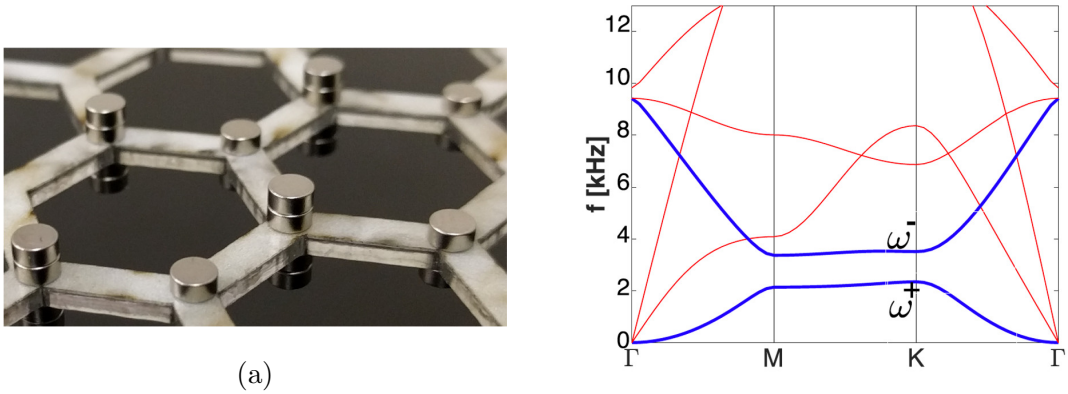

(a) (b)

FIG. 22: (a) Designed structure is a thin plate with hexagonal holes. Different masses are attached to the sub-lattice sites to break inversion symmetry. (b) Dispersion curves over the boundary of the IBZ for the unit cell. Blue curves are out of plane bending modes while red curves are in plane longitudinal and shear modes[88]. (Reproduced with permission from Phys. Rev. B 96, 134307 (2017). Copyright 2017 American Physical Society.)

these modes.

Figure 23 displays the dispersion diagram for a finite strip, calculated using the plane wave expansion method. The frequency is expressed in non-dimensional form by normalizing it as $\Omega = \omega\sqrt{EI/\rho A}$ and the wave vector is normalized by the unit cell length a. The modes are bounded by two curves $\Omega = \mu^2$ and $\Omega = \pi^2 - \mu^2$. This is because the group velocity at each frequency ω is bounded by the corresponding value for a homogeneous plate. Similar to the discrete case, there are two kinds of interface, depending on whether there are adjacent heavy or light masses at the junction. Figures 23c and 23d display the mode shapes at each kind of interface. These modes are called elastic valley modes and they span the bandgap frequencies for sufficiently small values of the mass difference. Note how they are localized at the interface and their amplitude decays rapidly away from it.

Let us now see an experimental demonstration of how such waves are able to navigate sharp bends without scattering losses. The structure is made of acrylic and magnetic cylinders are attached on both sides that attract each other. The unit cell size is 18.4 mm. The magnetic force between cylinders on adjacent lattice sites is assumed to be negligible. Figure 24a displays the experimental setup of an N-shaped topological waveguide realized by creating an interface. The red and cyan circles indicate locations with low and high

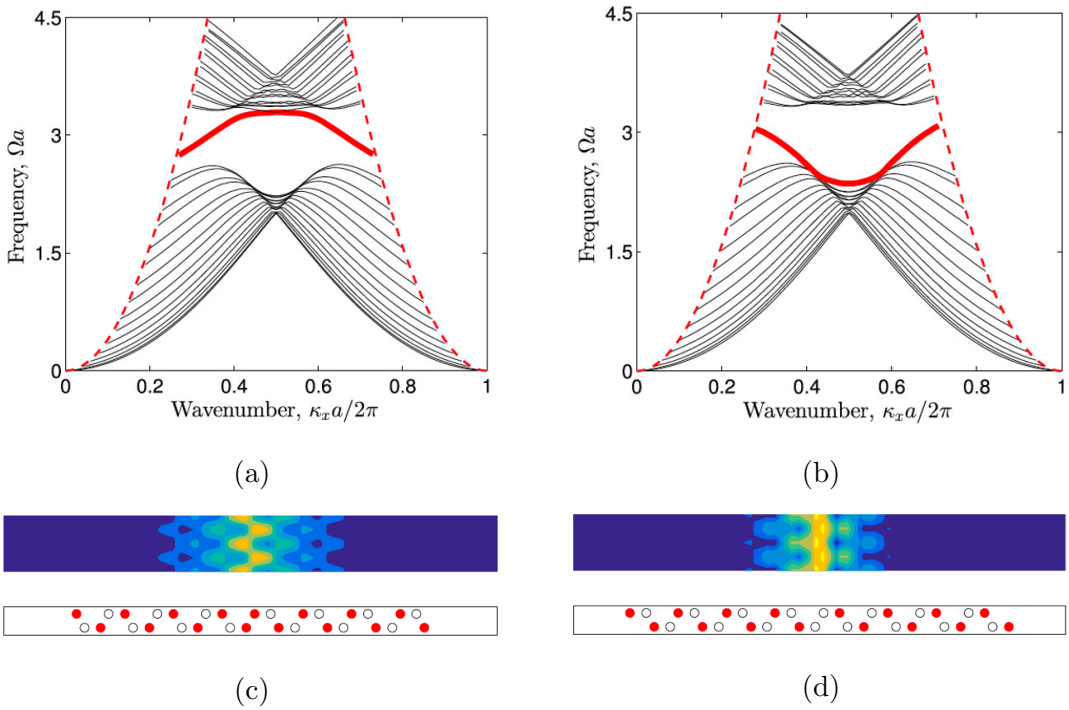

FIG. 23: Dispersion diagram for a finite strip having an interface with adjacent (a) light and (b) heavy masses. In both cases, a mode is localized at the interface with frequency in the bandgap. (c,d) Typical mode shapes of this mode and schematic of the finite strip[57].

masses, respectively. There are two adjacent light masses and the unit cells on each side are inverted copies of each other. The bottom end of the waveguide is excited with a windowed tone burst excitation and the velocity field is measured throughout the lattice with sufficient spacing between adjacent points using an SLDV. Figure 24b displays the amplitude of the out-of-plane velocity component after the waves have passed through. The wave decays in amplitude as the plate is made of acrylic, but an examination of the reconstructed temporal evolution of the dynamics shows the absence of back-scattering as the wave navigates corners.

As discussed earlier, topologically protected modes exist at the interface between lattices with distinct topological invariants. In this case, the relevant invariant is the valley Chern number. In contrast, if the lattices on both sides of an interface have identical invariants, then no modes are guaranteed to exist. Localized defect modes can exist, but they typically do not span the bandgap and these modes are sensitive to the geometry of the interface. Such interfaces are topologically trivial and are termed trivial waveguides. The following

example illustrates their dynamic behavior. The lattices on either side of the interface are identical in the structure of Fig. 24c. Hence the topological invariants of the two lattices are identical and this interface is a trivial waveguide. The corresponding transient response shows that no wave navigates the corners. Thus comparing its response with that of the topological case shows the efficacy and superiority of the topological waveguide.

This example shows how valley modes can be induced in continuous elastic media using architected thin plates. Such valley modes have also been demonstrated in several other systems, including in small scale structures[92,93], reconfigurable waveguides with shunted piezoelectric patches[91], in acoustic lattices with sound waves[94–96] and in plates with bolts or stubs[58,97].

B. Elastic spin Hall modes

In Sec. IV D, the key ideas behind the mechanical analogue of the quantum spin Hall effect were discussed in the case of discrete lattice-like structures. Recall that this effect leads to topological helical modes at boundaries. In this section, a general procedure or recipe to obtain helical topologically protected edge modes in continuous passive elastic waveguides is thoroughly detailed.

In principle, in the case of a system made of solely passive components, time-reversal symmetry is preserved, and a phononic analogue of chiral edge states is precluded. However, as proposed in the pioneering work of Mousavi et al.[98], helical edge modes can be achieved in passive elastic waveguides as well by exploiting the fact that various Lamb modes are characterized by different polarization. Specifically, they showed that guided symmetric (S0) and anti-symmetric (A0) modes in plates are excellent candidates to achieve an elastic version of the quantum spin Hall effect (i.e., designing a system supporting two effective spins for Lamb waves over a sufficiently broad bandwidth).

Geometry and material modifications, in general, affect the dispersion behavior and the associated band structure of plates. For example, breaking translation symmetry by introducing periodic holes or inclusions may open bandgaps, which, however, may not be complete and may therefore affect only some of the modes. The opening of bandgaps supporting topological modes also requires the structure to maintain a specific symmetry. The general procedure to obtain topologically protected helical edge modes in continuous elastic

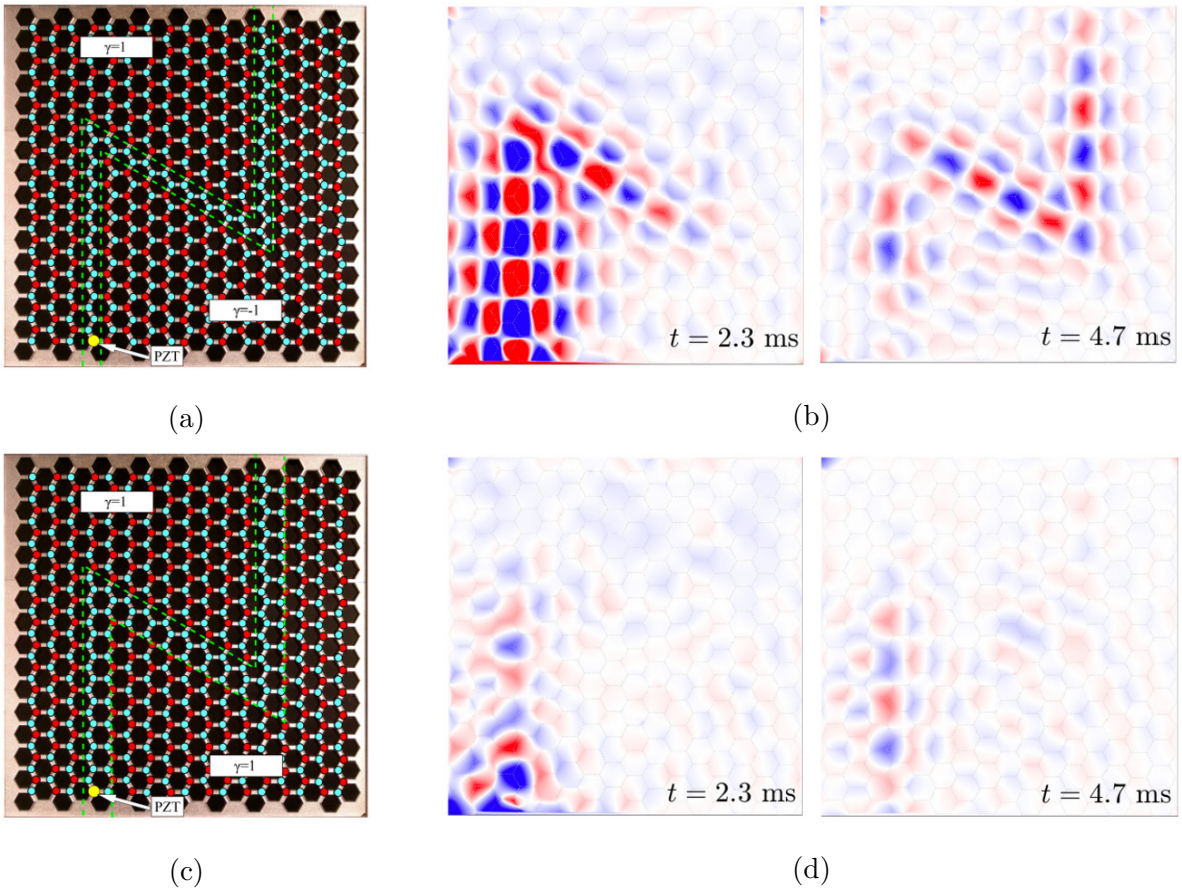

FIG. 24: N-shaped (a) topological and (c) trivial waveguide. Red and cyan circles have different mass amounts. (b,d): Their corresponding dynamic response at distinct time instants showing the wave navigates sharp bends in the topological waveguide[88]. (Reproduced with permission from Phys. Rev. B 96, 134307 (2017). Copyright 2017 American Physical Society.)

plates can be decomposed into the following steps:

- step 1 - Design a unit cell whose dispersion surfaces have an isolated double Dirac cone (Fig. 25);
- step 2 - Open a bandgap by breaking mid-plane symmetry of the unit cell (Fig. 26);
- step 3 - Create an interface using the unit cells of step 2. The unit cells on either side are mirror images of each other about the plate mid-plane. (Fig. 27a).

We will show below how applying the above steps to a patterned continuous elastic plate leads to helical topological protected edge modes. As mentioned, the first step is to create

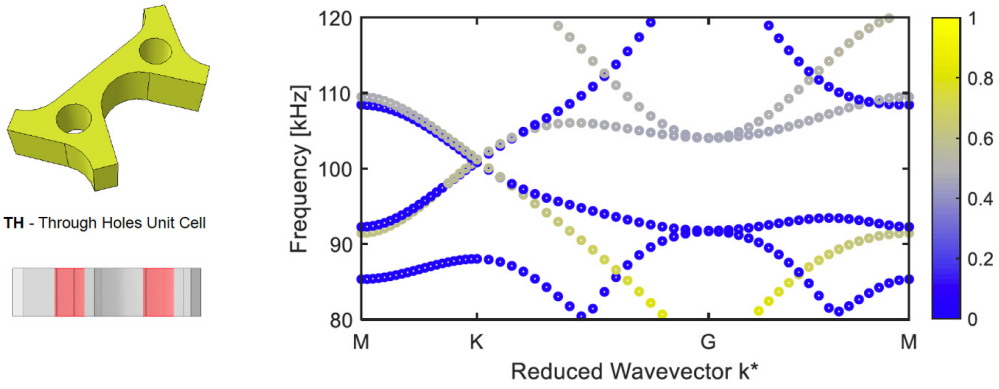

(a) (b)

FIG. 25: Step 1:(a) perspective and cross-sectional view of an architected unit cell with through the thickness holes - TH. (b) Its dispersion curves have a double Dirac cone and the corresponding modes have different polarization (in-plane and out-of-plane, represented respectively by the colors blue and grey/yellow in the right panel).

an isolated Dirac-like dispersion curves for the two polarized Lamb modes in the absence of σ_h symmetry (or reflection symmetry about the mid-plane of the plate) breaking. Let us consider an architected unit cell as the one showed in Fig. 25a. The specific patterning creates a graphene-like band structure for elastic waves. Specifically, the in-plane hexagonal symmetry provides Dirac dispersion for waves with an accidental degeneracy at K and K' points (Dirac points). While the plate geometrically resembles the twisted Kagome lattice described in[99], it is a continuous medium with no lumped elements such as point masses and springs can be identified. The associated dispersion surfaces have a double Dirac cone of modes with different polarization (in-plane and out-of-plane, represented respectively by the colors blue and grey/yellow in the right panel). Matching the frequency and the slope (group velocity) of Dirac cones associated with a symmetric mode and an anti-symmetric mode in a frequency range with no other modes is analogous to emulating the two spin states in graphene. Kane and Mele[81] showed that quantum spin Hall effect and helical edge modes arise when strong spin orbital coupling is introduced.

Once isolated double Dirac cones are achieved, a bandgap can be opened by by replacing the through-the-thickness holes by blind holes, i.e., holes not spanning the whole thickness of the plate, as illustrated in the perspective and cross-sectional view of Fig. 26a. Blind

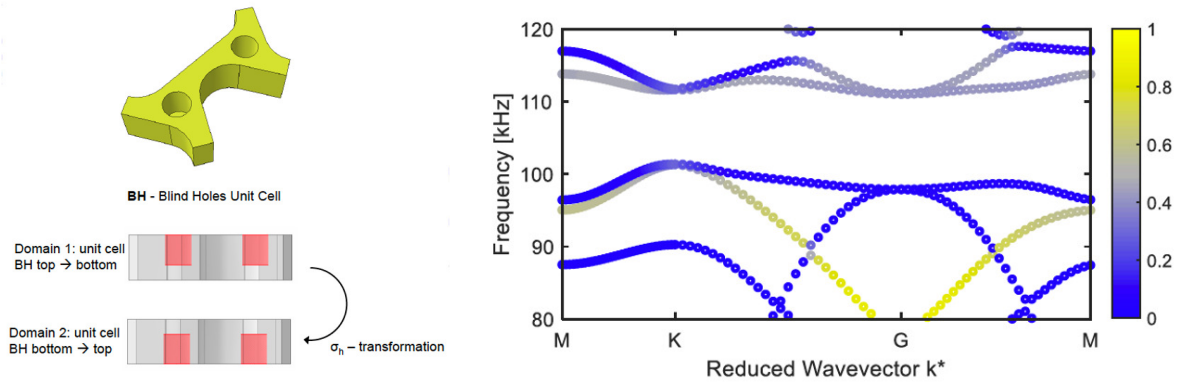

(a) (b)

FIG. 26: Step 2: (a) perspective and cross-sectional view of a unit cell with blind holes BH. Unit cells for domain 1 and domain 2 differ by a σ_h transformation, with blind holes being on the top vs bottom surface. (b) Modes are hybridized at the high symmetry point K, breaking σ_h symmetry.

holes (BH) through part of the plate thickness break the σ_h symmetry while preserving the original C_{3v} symmetry. This modification induces a coupling between the modes spanning the Dirac points: the in-plane polarized and out-of-plane polarized modes. This coupling is analogous to the spin orbital interaction in the quantum spin Hall effect. In contrast to valley modes where the two sets of modes are associated with two distinct valleys (K, K'), the spin Hall effect results from the hybridization of two distinct sets of modes spanning each of the high-symmetry K points.

This type of macroscopic geometrical modification produces a unit cell with broken σ_h symmetry, leading to mode hybridization at the high symmetry point K. Applying a σ_h-transformation to such a unit cell then gives the geometries for domain 1 and domain 2 (blind holes are inverted with respect to the mid-plane of the unit cell). The interface between them, as shown in the schematic in Fig. 27a is an elastic waveguide supporting localized helical edge modes in the bandgap frequencies. Figure 27b displays the numerical (white lines) and experimental measurements (energy spots) of the two distinct helical modes propagating in the waveguide. Experimental reconstruction of the helical edge modes characterized by a clockwise and counterclockwise variation of phase of the displacement field as the waves propagate from left to right. Fig. 27c illustrates a snapshot of the displacement

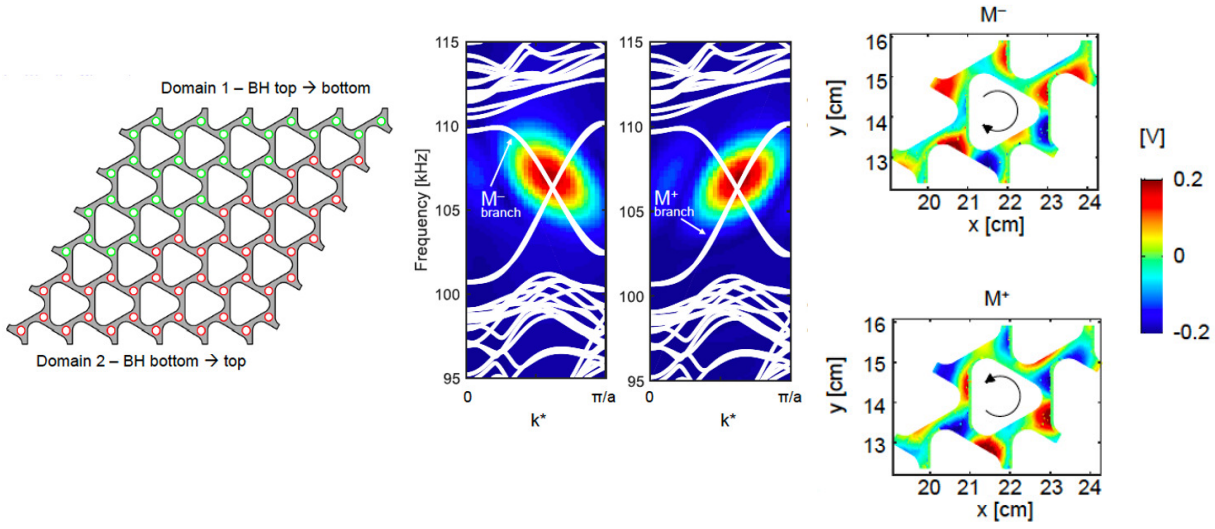

(a) (b) (c)

FIG. 27: Step 3: (a) schematic of a continuous elastic waveguide supporting helical modes at the interface between two unit cells related by a σ_h transformation. (b) Numerical (white lines) and experimental measurements (energy spots) of the two distinct helical modes. (c) Experimental reconstruction of the helical edge modes characterized by a clockwise and counterclockwise displacement phase field variation with respect to the direction of wave propagation (left to right)[16].

field. Refer to[16] for more details on the geometrical parameters of the unit cell and movie files of the experimental full field reconstruction. Hence there are two helical modes with opposite polarization. They have opposite group velocities for each wavenumber κ of waves propagating along the interface.

C. Combined valley and spin Hall modes

In this section we show how to design an elastic waveguide supporting multiple classes of edge modes (helical and valley). Specifically we will show a recipe to construct a continuous elastic waveguide capable of splitting equal-frequency helical edge waves differing on the basis of their polarization when they impinge on distinct interfaces at a common junction. The starting point is the same as for helical modes: a unit cell showing a double Dirac cone degeneracy, as the one examined in the previous section, and illustrated again in

Fig. 28a for clarity. From this unit cell, specific geometric modifications are introduced so as σ_v and σ_h symmetries, i.e., inversion and reflection symmetries, are selectively broken in specific portions of an elastic waveguide, as shown in Fig. 29a. The introduced geometric perturbations produce topological bandgaps that, respectively, support helical and valley modes in a common frequency range. Specifically, replacing the through holes of Fig. 28a with blind holes of 0.9 times the height of the plate, as shown in Fig. 28b, breaks the σ_h symmetry. We denote the configuration with the blind holes on the top (bottom) surface as H^+ (H^-). The interface between H^+ and H^- supports two helical edge modes spanning the gap with positive (Φ^+) and negative (Φ^-) group velocity, respectively (Fig. 29b).

Next, we break the σ_v symmetry or reflection symmetry about a vertical plane parallel to a lattice vector direction. This id done by making the holes in each unit cell of different radii, namely r and R (see Fig. 28c). Inverting the position of the larger and smaller radii allows us to identify two distinct unit cells, denoted as Vr and VR (Fig. 28c). Contrary to the previous case, an interface that separates two σ_v-transformed copies of the structure supports a single valley mode, with positive or negative group velocity, depending on the type of interface, i.e., with two adjacent holes of diameter r or R, respectively. Besides, the interfaces between structures supporting helical and valley modes will still support a single hybrid edge mode with either positive (Ψ^+) or negative (Ψ^-) group velocity, as shown in Figs. 29c,d. The edge modes are denoted by the index + (−) according to their positive (negative) group velocity when the wavenumber κ is in $[0, \pi/a]$. Note that this wavenumber is for waves propagating along an interface between two kinds of unit cells. In Figs. 29b-d, bulk modes are shaded in grey, while the edge states are denoted by the black, blue and red circles, depending on the types of interface: H^+/H^-), H^+/V^R), and H^-, V^r), respectively.

Finally, Figs. 30a,b show the numerical distribution of the von Mises stress field resulting from harmonic excitation at 98 kHz, i.e. within the bulk gap. The excitation is applied at the location shown by the white dot as an out-of-plane displacement distribution and the calculations clearly illustrate the possibility to preferentially excite one of the two modes and to remotely select the interface along which the wave will propagate once impinging the Y-shaped junction. Colors indicate the von Mises stress, ranging from zero (blue) to maximum (red). Refer to[90] for the geometrical details of the unit cells and further details. Such wave splitting shows the potential for novel elastic wave manipulation capabilities.

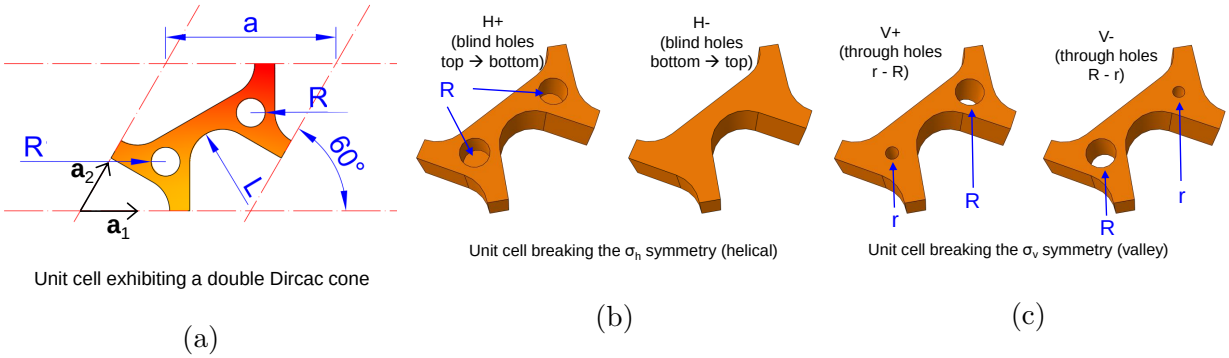

FIG. 28: (a) Top view of the designed unit cell with through-the-thickness holes whose dispersion has a double Dirac cone (see Fig. 25b). (b) Perspective view of two unit cells with broken σ_h symmetry. H+ has blind holes on the top surface and H- has blind holes at the bottom. They both break Dirac cones and open a bandgap (see Fig. 26b). (c) Perspective view of the unit cells with broken σ_v symmetry. V+ and V- had different size through holes. Both unit cells also open a bandgap in the same frequency range.

VI. OUTLOOK AND FUTURE DIRECTIONS

The past decade has seen an explosive growth in this research field, motivated by both an exploration of fundamental wave phenomena in elastic media and aimed at specific technological applications. The key realization in our opinion is that interfaces and defect modes can be designed in a systematic way by incorporating features derived from topological considerations. The examples discussed above showed how one can achieve robust and backscattering free waveguides that have sharp bends and corners. Different dimensions exhibit distinct topological phenomena: for instance the existence of a non-zero Zak phase in $1D$ systems and Weyl points in $3D$ systems. In this article, we have primarily focused on topological phenomena in elastic beams and plates that can be characterized by a Chern number. Now, let us we outline some promising future research directions.

Reconfigurable waveguides[83,100] are just beginning to be explored and remain to be realized in a variety of elastic waveguides. Similarly, multiphysics interactions, including between elastic and electromagnetic domains, for example in piezoelectric media[101,102], or between fluids and structures[103], may open avenues for controlling waves in one media with another. Extending unit cell designs to three dimensional periodic structures will significantly expand the design space as well as allow for $3D$ manipulation and control of elastic waves. They may

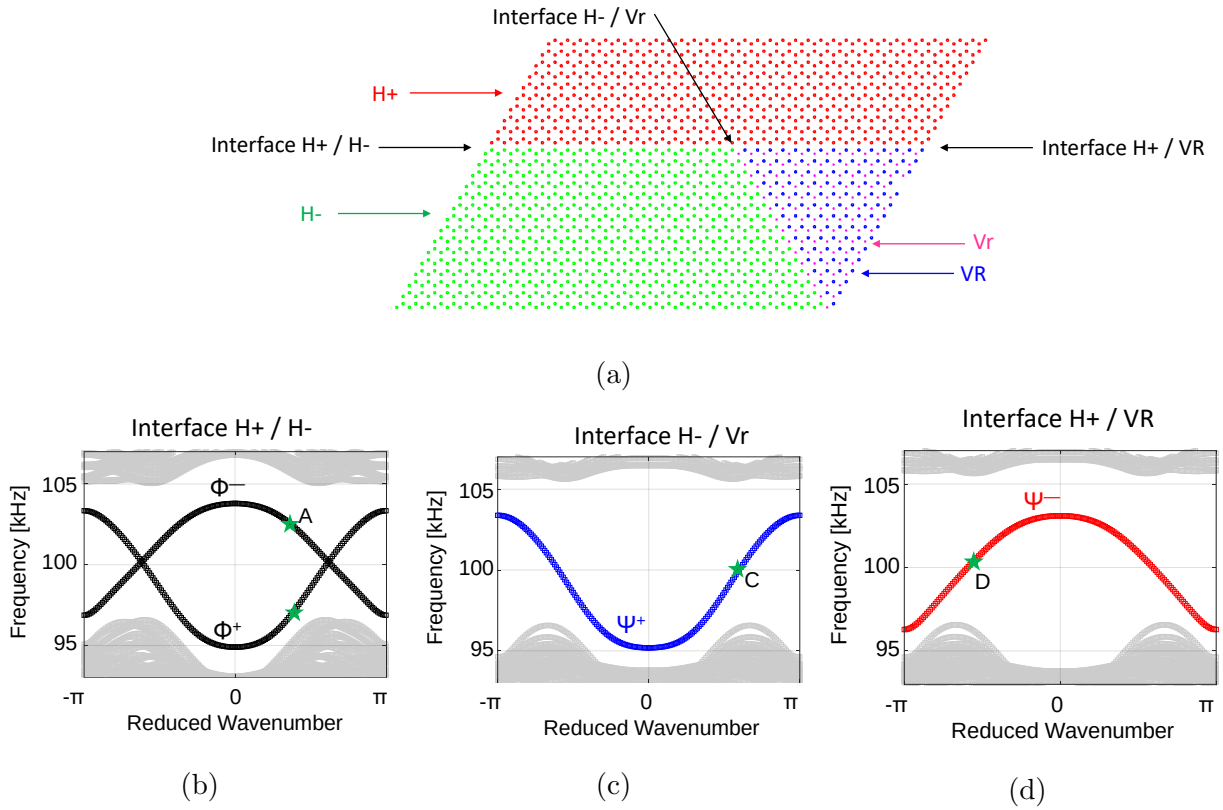

FIG. 29: (a) Digital model to assist the drilling machine for the manufacturing of the waveguide. Holes in red (green) define the H^+ (H^-) unit cell where blind holes are drilled. Hole depth is 0.9 times the height of the plate. Holes in blue (violet) define the V^R (V^r) unit cells where holes are drilled through the whole thickness of the plate, but that have different radii. (b - d) Dispersion diagrams for non-trivial stripes with the following types of interfaces: H^+/H^-), H^+/V^R), and H^-, V^r), respectively. The band structures are computed considering the strips periodic in the horizontal direction and made of 10 unit cells on each side of the domain wall. The bulk modes are reported as gray dots while the interface modes in black, blue and red dotted lines, respectively. The edge modes are denoted by the index + (−) according to their positive (negative) group velocity with respect to the propagation direction[90]. (Reproduced with permission from Phys. Rev. B 100, 024304 (2019). Copyright 2019 American Physical Society.)

allow for exploiting Weyl points[104] or can realize constructions like fragile topology[105] that exhibit spectral flow at interfaces. Similarly, quasiperiodic[106,107] and non-periodic[108] metastructures offer rich opportunities for achieving unique static and dynamic behaviors. Such

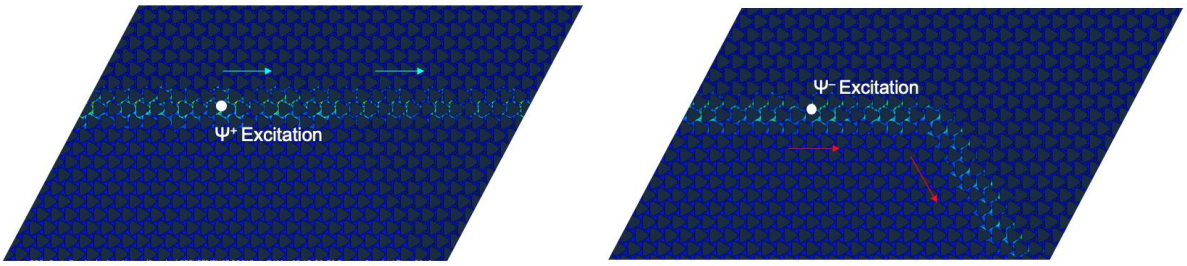

(a) (b)

FIG. 30: (a - b) Numerical distribution of the von Mises stress field resulting from harmonic excitation at 98 kHz, i.e. within the bulk gap. The excitation is applied at the location shown by the white dot as an out-of-plane displacement. The calculations illustrate the possibility of preferentially exciting one of the two modes and of thus remotely selecting the interface along which the wave will propagate after it impinges on the Y-shaped junction.

concepts have recently started to be investigated in static media and in $1D$ beam systems. Extending unit cell concepts to non-periodic, complex geometries[109], higher dimensions and higher order topological modes[110] will open avenues for unique wave manipulation properties. In particular, quasi- and non-periodic structures exhibit for bulk isotropic behavior as opposed to anisotropic behavior that is associated with periodic media, for example C_3, C_4 media in $2D$ structures.

On the theoretical side, several questions similarly remain unanswered, having to do with the role of nonlinearities. Notably, nonlinear[111–113] and non-Hermitian[114–116] elastic structures have exciting potential for realizing novel wave phenomena. The topological properties of such systems remain to be investigated and they may allow for solitons, frequency conversion, localized skin modes, unidirectional reflection in elastic structures like beams, plates and shells[117,118]. In this regard, the advent of $3D$[119] and $4D$ printing[120,121] has opened novel avenues for fabricating complex shaped structures that were beyond the reach of conventional manufacturing methods. Synthetic high dimensional spaces have been created in other physical domains by modulating geometric parameters in time[122] or by accessing additional degrees of freedom[123]. Such techniques can lead to the realization of topological wave phenomena associated with the corresponding higher dimensions in elastic media too. We anticipate that these directions will thus lead to fruitful fundamental and applied research

in the coming years and will lead to the discovery of novel and exciting effects in the domain of topological elastic waves.

ACKNOWLEDGMENTS

MM is funded by the European Union's Horizon 2020 FET Open ("Boheme") under grant agreement No. 863179. RKP is supported by startup funds from Kansas State University and by U.S National Science Foundation Award No. 2027455.

DATA AVAILABILITY

The data that support the findings of this study are available from the corresponding author upon reasonable request.

REFERENCES

[1]R. Courant and D. Hilbert, *Methods of mathematical physics: partial differential equations* (John Wiley & Sons, 2008).

[2]C. Kittel, P. McEuen, and P. McEuen, *Introduction to solid state physics*, Vol. 8 (Wiley New York, 1996).

[3]L. Brillouin, *Wave propagation and group velocity*, Vol. 8 (Academic press, 2013).

[4]J. D. Jackson, "Classical electrodynamics," (1999).

[5]X. Zhang, M. Xiao, Y. Cheng, M.-H. Lu, and J. Christensen, "Topological sound," Communications Physics **1**, 1–13 (2018).

[6]V. Giurgiutiu, *Structural health monitoring: with piezoelectric wafer active sensors* (Elsevier, 2007).

[7]W. Ostachowicz, P. Kudela, M. Krawczuk, and A. Zak, *Guided waves in structures for SHM: the time-domain spectral element method* (John Wiley & Sons, 2011).

[8]J. L. Rose, *Ultrasonic guided waves in solid media* (Cambridge university press, 2014).

[9]P. A. Deymier, *Acoustic metamaterials and phononic crystals*, Vol. 173 (Springer Science & Business Media, 2013).

[10]M. Z. Hasan and C. L. Kane, "Colloquium: topological insulators," Reviews of modern physics **82**, 3045 (2010).

[11]L. Lu, J. D. Joannopoulos, and M. Soljačić, "Topological photonics," Nature photonics **8**, 821–829 (2014).

[12]P. Di Pietro, M. Ortolani, O. Limaj, A. Di Gaspare, V. Giliberti, F. Giorgianni, M. Brahlek, N. Bansal, N. Koirala, S. Oh, *et al.*, "Observation of dirac plasmons in a topological insulator," Nature nanotechnology **8**, 556–560 (2013).

[13]C. He, X. Ni, H. Ge, X.-C. Sun, Y.-B. Chen, M.-H. Lu, X.-P. Liu, and Y.-F. Chen, "Acoustic topological insulator and robust one-way sound transport," Nature physics **12**, 1124–1129 (2016).

[14]J. Cha, K. W. Kim, and C. Daraio, "Experimental realization of on-chip topological nanoelectromechanical metamaterials," Nature **564**, 229–233 (2018).

[15]E. Prodan and C. Prodan, "Topological phonon modes and their role in dynamic instability of microtubules," Physical review letters **103**, 248101 (2009).

[16]M. Miniaci, R. Pal, B. Morvan, and M. Ruzzene, "Experimental observation of topologically protected helical edge modes in patterned elastic plates," Physical Review X **8**, 031074 (2018).

[17]B.-Z. Xia, T.-T. Liu, G.-L. Huang, H.-Q. Dai, J.-R. Jiao, X.-G. Zang, D.-J. Yu, S.-J. Zheng, and J. Liu, "Topological phononic insulator with robust pseudospin-dependent transport," Physical Review B **96**, 094106 (2017).

[18]J. Ma, D. Zhou, K. Sun, X. Mao, and S. Gonella, "Edge modes and asymmetric wave transport in topological lattices: Experimental characterization at finite frequencies," Physical review letters **121**, 094301 (2018).

[19]Y. Barlas and E. Prodan, "Topological classification table implemented with classical passive metamaterials," Physical Review B **98**, 094310 (2018).

[20]O. B. Wright and O. Matsuda, "Watching surface waves in phononic crystals," Philosophical Transactions of the Royal Society A: Mathematical, Physical and Engineering Sciences **373**, 20140364 (2015).

[21]T. Ma, A. B. Khanikaev, S. H. Mousavi, and G. Shvets, "Guiding electromagnetic waves around sharp corners: topologically protected photonic transport in metawaveguides," Physical review letters **114**, 127401 (2015).

[22]L. M. Nash, D. Kleckner, A. Read, V. Vitelli, A. M. Turner, and W. T. Irvine, "Topological mechanics of gyroscopic metamaterials," Proceedings of the National Academy of Sciences **112**, 14495–14500 (2015).

[23]P. Wang, L. Lu, and K. Bertoldi, "Topological phononic crystals with one-way elastic edge waves," Physical review letters **115**, 104302 (2015).

[24]R. Süsstrunk and S. D. Huber, "Observation of phononic helical edge states in a mechanical topological insulator," Science **349**, 47–50 (2015).

[25]R. K. Pal, M. Schaeffer, and M. Ruzzene, "Helical edge states and topological phase transitions in phononic systems using bi-layered lattices," Journal of Applied Physics **119**, 084305 (2016).

[26]C. Kane and T. Lubensky, "Topological boundary modes in isostatic lattices," Nature Physics **10**, 39–45 (2014).

[27]D. Z. Rocklin, B. G.-g. Chen, M. Falk, V. Vitelli, and T. Lubensky, "Mechanical weyl modes in topological maxwell lattices," Physical review letters **116**, 135503 (2016).

[28]D. Z. Rocklin, S. Zhou, K. Sun, and X. Mao, "Transformable topological mechanical metamaterials," Nature communications **8**, 1–9 (2017).

[29]Y. Jin, D. Torrent, and B. Djafari-Rouhani, "Robustness of conventional and topologically protected edge states in phononic crystal plates," Physical Review B **98**, 054307 (2018).

[30]L. He, Z. Wen, Y. Jin, D. Torrent, X. Zhuang, and T. Rabczuk, "Inverse design of topological metaplates for flexural waves with machine learning," Materials & Design **199**, 109390 (2021).

[31]K. H. Matlack, M. Serra-Garcia, A. Palermo, S. D. Huber, and C. Daraio, "Designing perturbative metamaterials from discrete models," Nature materials **17**, 323–328 (2018).

[32]D. Royer and E. Dieulesaint, *Elastic waves in solids I: Free and guided propagation* (Springer Science & Business Media, 1999).

[33]J. Achenbach, *Wave propagation in elastic solids* (Elsevier, 2012).

[34]K. F. Graff, *Wave motion in elastic solids* (Courier Corporation, 2012).

[35]A. H. Nayfeh, *Wave propagation in layered anisotropic media: With application to composites* (Elsevier, 1995).

[36]B. A. Auld, *Acoustic fields and waves in solids, volumes 1 and 2* (John Wiley, New York and London, 1973).

[37]D. Royer and E. Dieulesaint, *Elastic waves in solids II: generation, acousto-optic interaction, applications* (Springer Science & Business Media, 1999).

[38]A. Preumont, *Vibration control of active structures: an introduction*, Vol. 246 (Springer, 2018).

[39]G. Trainiti and M. Ruzzene, "Non-reciprocal elastic wave propagation in spatiotemporal periodic structures," New Journal of Physics **18**, 083047 (2016).

[40]C. Croënne, J. Vasseur, O. Bou Matar, M.-F. Ponge, P. A. Deymier, A.-C. Hladky-Hennion, and B. Dubus, "Brillouin scattering-like effect and non-reciprocal propagation of elastic waves due to spatio-temporal modulation of electrical boundary conditions in piezoelectric media," Applied Physics Letters **110**, 061901 (2017).

[41]A. Merkel, M. Willatzen, and J. Christensen, "Dynamic nonreciprocity in loss-compensated piezophononic media," Physical Review Applied **9**, 034033 (2018).

[42]C. Croënne, J. Vasseur, O. Bou Matar, A.-C. Hladky-Hennion, and B. Dubus, "Non-reciprocal behavior of one-dimensional piezoelectric structures with space-time modulated electrical boundary conditions," Journal of Applied Physics **126**, 145108 (2019).

[43]F. Ruesink, M.-A. Miri, A. Alu, and E. Verhagen, "Nonreciprocity and magnetic-free isolation based on optomechanical interactions," Nature communications **7**, 1–8 (2016).

[44]Y. Hadad, J. C. Soric, and A. Alu, "Breaking temporal symmetries for emission and absorption," Proceedings of the National Academy of Sciences **113**, 3471–3475 (2016).

[45]H. Nassar, B. Yousefzadeh, R. Fleury, M. Ruzzene, A. Alù, C. Daraio, A. N. Norris, G. Huang, and M. R. Haberman, "Nonreciprocity in acoustic and elastic materials," Nature Reviews Materials **5**, 667–685 (2020).

[46]L. R. Meza, A. J. Zelhofer, N. Clarke, A. J. Mateos, D. M. Kochmann, and J. R. Greer, "Resilient 3d hierarchical architected metamaterials," Proceedings of the National Academy of Sciences **112**, 11502–11507 (2015).

[47]M. Miniaci, A. Krushynska, A. S. Gliozzi, N. Kherraz, F. Bosia, and N. M. Pugno, "Design and fabrication of bioinspired hierarchical dissipative elastic metamaterials," Physical Review Applied **10**, 024012 (2018).

[48]D. Bigoni, S. Guenneau, A. B. Movchan, and M. Brun, "Elastic metamaterials with inertial locally resonant structures: Application to lensing and localization," Physical Review B **87**, 174303 (2013).

[49]R. V. Craster and S. Guenneau, *Acoustic metamaterials: Negative refraction, imaging, lensing and cloaking*, Vol. 166 (Springer Science & Business Media, 2012).

[50]D. Tallarico, G. Hannema, M. Miniaci, A. Bergamini, A. Zemp, and B. Van Damme, "Superelement modelling of elastic metamaterials: Complex dispersive properties of three-dimensional structured beams and plates," Journal of Sound and Vibration , 115499 (2020).

[51]M. Mazzotti, M. Miniaci, and I. Bartoli, "Band structure analysis of leaky bloch waves in 2d phononic crystal plates," Ultrasonics **74**, 140–143 (2017).

[52]M. Miniaci, A. S. Gliozzi, B. Morvan, A. Krushynska, F. Bosia, M. Scalerandi, and N. M. Pugno, "Proof of concept for an ultrasensitive technique to detect and localize sources of elastic nonlinearity using phononic crystals," Physical review letters **118**, 214301 (2017).

[53]Z. Liu, X. Zhang, Y. Mao, Y. Zhu, Z. Yang, C. T. Chan, and P. Sheng, "Locally resonant sonic materials," science **289**, 1734–1736 (2000).

[54]M. S. Kushwaha, P. Halevi, L. Dobrzynski, and B. Djafari-Rouhani, "Acoustic band structure of periodic elastic composites," Physical review letters **71**, 2022 (1993).

[55]Y. Tanaka and S.-i. Tamura, "Acoustic stop bands of surface and bulk modes in two-dimensional phononic lattices consisting of aluminum and a polymer," Physical Review B **60**, 13294 (1999).

[56]D. Torrent, D. Mayou, and J. Sánchez-Dehesa, "Elastic analog of graphene: Dirac cones and edge states for flexural waves in thin plates," Physical Review B **87**, 115143 (2013).

[57]R. K. Pal and M. Ruzzene, "Edge waves in plates with resonators: an elastic analogue of the quantum valley hall effect," New Journal of Physics **19**, 025001 (2017).

[58]R. Chaunsali, C.-W. Chen, and J. Yang, "Subwavelength and directional control of flexural waves in zone-folding induced topological plates," Physical Review B **97**, 054307 (2018).

[59]V. Dal Poggetto and A. L. Serpa, "Elastic wave band gaps in a three-dimensional periodic metamaterial using the plane wave expansion method," International Journal of Mechanical Sciences **184**, 105841 (2020).

[60]S. Benchabane, A. Khelif, J.-Y. Rauch, L. Robert, and V. Laude, "Evidence for complete surface wave band gap in a piezoelectric phononic crystal," Physical Review E **73**, 065601 (2006).

[61]Z. Hou and B. M. Assouar, "Modeling of lamb wave propagation in plate with two-dimensional phononic crystal layer coated on uniform substrate using plane-wave-

expansion method," Physics Letters A **372**, 2091–2097 (2008).

[62]V. Laude, Y. Achaoui, S. Benchabane, and A. Khelif, "Evanescent bloch waves and the complex band structure of phononic crystals," Physical Review B **80**, 092301 (2009).

[63]M. Oudich and M. Badreddine Assouar, "Complex band structures and evanescent bloch waves in two-dimensional finite phononic plate," Journal of Applied Physics **112**, 104509 (2012).

[64]T. J. Hughes, *The finite element method: linear static and dynamic finite element analysis* (Courier Corporation, 2012).

[65]M. Åberg and P. Gudmundson, "The usage of standard finite element codes for computation of dispersion relations in materials with periodic microstructure," The Journal of the Acoustical Society of America **102**, 2007–2013 (1997).

[66]O. C. Zienkiewicz, R. L. Taylor, and J. Z. Zhu, *The finite element method: its basis and fundamentals* (Elsevier, 2005).

[67]A. Spadoni, M. Ruzzene, S. Gonella, and F. Scarpa, "Phononic properties of hexagonal chiral lattices," Wave motion **46**, 435–450 (2009).

[68]S. D. Huber, "Topological mechanics," Nature Physics **12**, 621–623 (2016).

[69]R. K. Pal, M. I. Rosa, and M. Ruzzene, "Topological bands and localized vibration modes in quasiperiodic beams," New Journal of Physics **21**, 093017 (2019).

[70]H. Chen, H. Nassar, and G. Huang, "A study of topological effects in 1d and 2d mechanical lattices," Journal of the Mechanics and Physics of Solids **117**, 22–36 (2018).

[71]W. Su, J. Schrieffer, and A. J. Heeger, "Solitons in polyacetylene," Physical review letters **42**, 1698 (1979).

[72]D. Thouless, "Quantization of particle transport," Physical Review B **27**, 6083 (1983).

[73]D. J. Thouless, M. Kohmoto, M. P. Nightingale, and M. den Nijs, "Quantized hall conductance in a two-dimensional periodic potential," Physical review letters **49**, 405 (1982).

[74]M. I. Rosa, R. K. Pal, J. R. Arruda, and M. Ruzzene, "Edge states and topological pumping in spatially modulated elastic lattices," Physical review letters **123**, 034301 (2019).

[75]M. Nakahara, *Geometry, topology and physics* (CRC Press, 2003).

[76]C. Nash and S. Sen, *Topology and geometry for physicists* (Elsevier, 1988).

[77]E. Prodan and H. Schulz-Baldes, "Bulk and boundary invariants for complex topological insulators," K (2016).

[78]E. Riva, M. I. Rosa, and M. Ruzzene, "Edge states and topological pumping in stiffness-modulated elastic plates," Physical Review B **101**, 094307 (2020).

[79]F. D. M. Haldane, "Model for a quantum hall effect without landau levels: Condensed-matter realization of the" parity anomaly"," Physical review letters **61**, 2015 (1988).

[80]M. I. Hussein, M. J. Leamy, and M. Ruzzene, "Dynamics of phononic materials and structures: Historical origins, recent progress, and future outlook," Applied Mechanics Reviews **66** (2014).

[81]C. L. Kane and E. J. Mele, "Quantum spin hall effect in graphene," Physical review letters **95**, 226801 (2005).

[82]H. Chen, H. Nassar, A. N. Norris, G. Hu, and G. Huang, "Elastic quantum spin hall effect in kagome lattices," Physical Review B **98**, 094302 (2018).

[83]T.-W. Liu and F. Semperlotti, "Tunable acoustic valley–hall edge states in reconfigurable phononic elastic waveguides," Physical Review Applied **9**, 014001 (2018).

[84]M. Yan, J. Lu, F. Li, W. Deng, X. Huang, J. Ma, and Z. Liu, "On-chip valley topological materials for elastic wave manipulation," Nature Materials **17**, 993–998 (2018).

[85]K. Qian, D. J. Apigo, C. Prodan, Y. Barlas, and E. Prodan, "Topology of the valley-chern effect," Physical Review B **98**, 155138 (2018).

[86]J. Ma, K. Sun, and S. Gonella, "Valley hall in-plane edge states as building blocks for elastodynamic logic circuits," Physical Review Applied **12**, 044015 (2019).

[87]A. C. Neto, F. Guinea, N. M. Peres, K. S. Novoselov, and A. K. Geim, "The electronic properties of graphene," Reviews of modern physics **81**, 109 (2009).

[88]J. Vila, R. K. Pal, and M. Ruzzene, "Observation of topological valley modes in an elastic hexagonal lattice," Physical Review B **96**, 134307 (2017).

[89]M. A. Hasan, L. Calderin, P. Lucas, K. Runge, and P. A. Deymier, "Spectral analysis of amplitudes and phases of elastic waves: Application to topological elasticity," The Journal of the Acoustical Society of America **146**, 748–766 (2019).

[90]M. Miniaci, R. K. Pal, R. Manna, and M. Ruzzene, "Valley-based splitting of topologically protected helical waves in elastic plates," Physical Review B **100**, 024304 (2019).

[91]A. Darabi, M. Collet, and M. J. Leamy, "Experimental realization of a reconfigurable electroacoustic topological insulator," Proceedings of the National Academy of Sciences **117**, 16138–16142 (2020).

[92]X.-T. He, E.-T. Liang, J.-J. Yuan, H.-Y. Qiu, X.-D. Chen, F.-L. Zhao, and J.-W. Dong, "A silicon-on-insulator slab for topological valley transport," Nature communications **10**, 1–9 (2019).

[93]C. Brendel, V. Peano, O. Painter, and F. Marquardt, "Snowflake phononic topological insulator at the nanoscale," Physical Review B **97**, 020102 (2018).

[94]J. Lu, C. Qiu, L. Ye, X. Fan, M. Ke, F. Zhang, and Z. Liu, "Observation of topological valley transport of sound in sonic crystals," Nature Physics **13**, 369–374 (2017).

[95]J. Lu, C. Qiu, M. Ke, and Z. Liu, "Valley vortex states in sonic crystals," Physical review letters **116**, 093901 (2016).

[96]J. Lu, C. Qiu, W. Deng, X. Huang, F. Li, F. Zhang, S. Chen, and Z. Liu, "Valley topological phases in bilayer sonic crystals," Physical review letters **120**, 116802 (2018).

[97]R. Chaunsali, C.-W. Chen, and J. Yang, "Experimental demonstration of topological waveguiding in elastic plates with local resonators," New Journal of Physics **20**, 113036 (2018).

[98]S. H. Mousavi, A. B. Khanikaev, and Z. Wang, "Topologically protected elastic waves in phononic metamaterials," Nature communications **6**, 1–7 (2015).

[99]T. Lubensky, C. Kane, X. Mao, A. Souslov, and K. Sun, "Phonons and elasticity in critically coordinated lattices," Reports on Progress in Physics **78**, 073901 (2015).

[100]D. Zhou, J. Ma, K. Sun, S. Gonella, and X. Mao, "Switchable phonon diodes using nonlinear topological maxwell lattices," Physical Review B **101**, 104106 (2020).

[101]C. Sugino, S. Leadenham, M. Ruzzene, and A. Erturk, "An investigation of electroelastic bandgap formation in locally resonant piezoelectric metastructures," Smart Materials and Structures **26**, 055029 (2017).

[102]C. Sugino, M. Ruzzene, and A. Erturk, "Nonreciprocal piezoelectric metamaterial framework and circuit strategies," Physical Review B **102**, 014304 (2020).

[103]M. I. Hussein, S. Biringen, O. R. Bilal, and A. Kucala, "Flow stabilization by subsurface phonons," Proceedings of the Royal Society A: Mathematical, Physical and Engineering Sciences **471**, 20140928 (2015).

[104]V. Peri, M. Serra-Garcia, R. Ilan, and S. D. Huber, "Axial-field-induced chiral channels in an acoustic weyl system," Nature Physics **15**, 357–361 (2019).

[105]V. Peri, Z.-D. Song, M. Serra-Garcia, P. Engeler, R. Queiroz, X. Huang, W. Deng, Z. Liu, B. A. Bernevig, and S. D. Huber, "Experimental characterization of fragile topology in

an acoustic metamaterial," Science **367**, 797–800 (2020).

[106]D. J. Apigo, W. Cheng, K. F. Dobiszewski, E. Prodan, and C. Prodan, "Observation of topological edge modes in a quasiperiodic acoustic waveguide," Physical review letters **122**, 095501 (2019).

[107]Y. Xia, A. Erturk, and M. Ruzzene, "Topological edge states in quasiperiodic locally resonant metastructures," Physical Review Applied **13**, 014023 (2020).

[108]N. P. Mitchell, L. M. Nash, D. Hexner, A. M. Turner, and W. T. Irvine, "Amorphous topological insulators constructed from random point sets," Nature Physics **14**, 380–385 (2018).

[109]A. Foehr, O. R. Bilal, S. D. Huber, and C. Daraio, "Spiral-based phononic plates: From wave beaming to topological insulators," Physical review letters **120**, 205501 (2018).

[110]H. Fan, B. Xia, L. Tong, S. Zheng, and D. Yu, "Elastic higher-order topological insulator with topologically protected corner states," Physical review letters **122**, 204301 (2019).

[111]R. Chaunsali and G. Theocharis, "Self-induced topological transition in phononic crystals by nonlinearity management," Physical Review B **100**, 014302 (2019).

[112]B. Deng, J. Raney, V. Tournat, and K. Bertoldi, "Elastic vector solitons in soft architected materials," Physical review letters **118**, 204102 (2017).

[113]L. Jin, R. Khajehtourian, J. Mueller, A. Rafsanjani, V. Tournat, K. Bertoldi, and D. M. Kochmann, "Guided transition waves in multistable mechanical metamaterials," Proceedings of the National Academy of Sciences **117**, 2319–2325 (2020).

[114]C. Scheibner, W. T. Irvine, and V. Vitelli, "Non-hermitian band topology and skin modes in active elastic media," Physical Review Letters **125**, 118001 (2020).

[115]A. Ghatak, M. Brandenbourger, J. van Wezel, and C. Coulais, "Observation of non-hermitian topology and its bulk–edge correspondence in an active mechanical metamaterial," Proceedings of the National Academy of Sciences **117**, 29561–29568 (2020).

[116]M. I. Rosa and M. Ruzzene, "Dynamics and topology of non-hermitian elastic lattices with non-local feedback control interactions," New Journal of Physics **22**, 053004 (2020).

[117]S. Yao and Z. Wang, "Edge states and topological invariants of non-hermitian systems," Physical review letters **121**, 086803 (2018).

[118]Z. Gong, Y. Ashida, K. Kawabata, K. Takasan, S. Higashikawa, and M. Ueda, "Topological phases of non-hermitian systems," Physical Review X **8**, 031079 (2018).

[119]K. H. Matlack, A. Bauhofer, S. Krödel, A. Palermo, and C. Daraio, "Composite 3d-printed metastructures for low-frequency and broadband vibration absorption," Proceedings of the National Academy of Sciences **113**, 8386–8390 (2016).

[120]Q. Ge, C. K. Dunn, H. J. Qi, and M. L. Dunn, "Active origami by 4d printing," Smart materials and structures **23**, 094007 (2014).

[121]A. S. Gladman, E. A. Matsumoto, R. G. Nuzzo, L. Mahadevan, and J. A. Lewis, "Biomimetic 4d printing," Nature materials **15**, 413–418 (2016).

[122]X. Xu, Q. Wu, H. Chen, H. Nassar, Y. Chen, A. Norris, M. R. Haberman, and G. Huang, "Physical observation of a robust acoustic pumping in waveguides with dynamic boundary," Phys. Rev. Lett. **125**, 253901 (2020).

[123]E. Lustig, S. Weimann, Y. Plotnik, Y. Lumer, M. A. Bandres, A. Szameit, and M. Segev, "Photonic topological insulator in synthetic dimensions," Nature **567**, 356–360 (2019).